Mapping snow density through thermal inertia observations

[(1)*]Colombo R., [(1)]Pennati G., [(1)]Pozzi G., [(1)]Garzonio R., [(2)]Di Mauro B., [(3)]Giardino C. [(1)]Cogliati S., [(1)]Rossini M., [(4)]Maltese A., [(5)]Pogliotti P., [(5)]Cremonese E.

(1) Earth and Environmental Sciences Department, University of Milano-Bicocca, Milan (Italy)

(2) Institute of Polar Sciences, National Research Council, Milan (Italy)

(3) CNR-IREA, Milan (Italy)

(4) Engineering Department, University of Palermo, Palermo, Italy,

(5) Climate Change Unit, Environmental Protection Agency of Aosta Valley, Aosta (Italy)

*Corresponding author: Roberto.colombo@unimib.it, +39-0264482819, Remote Sensing of Environmental Dynamics Lab., DISAT, University of Milano-Bicocca, P.zza della Scienza 1, 20126, Milano, Italy.

Keywords

Thermal inertia, snow density, Landsat images, meteorological data, mountainous areas.

Highlights

- Snow thermal inertia reflects the status of the snowpack evolution;
- An empirical regression model is presented for mapping snow density from thermal inertia;
- This study can pave new perspectives in remote sensing of the cryosphere.

Abstract

Snow, as a fundamental reservoir of freshwater, is a crucial natural resource. Specifically, knowledge of snow density spatial and temporal variability could improve modelling of snow water equivalent, which is relevant for managing freshwater resources in context of ongoing climate change. The possibility of estimating snow density from remote sensing has great potential, considering the availability of satellite data and their ability to generate efficient monitoring systems from space.

In this study, we present an innovative method that combines meteorological parameters, satellite data and field snow measurements to estimate thermal inertia of snow and snow density at a catchment scale. Thermal inertia represents the responsiveness of a material to variations in temperature and depends on the thermal conductivity, density and specific heat of the medium. By exploiting Landsat 8 data and meteorological modelling, we generated multitemporal thermal inertia maps in mountainous catchments in the Western European Alps (Aosta Valley, Italy), from incoming shortwave radiation, surface temperature and snow albedo. Thermal inertia was then used to develop an empirical regression model to infer snow density, demonstrating the possibility of mapping snow density from optical and thermal observations from space. The model allows for estimation of snow density with R^2_{CV} and $RMSE_{CV}$ of 0.59 and 82 $\mathrm{kg\,m^{-3}}$, respectively. Thermal inertia and snow density maps are presented in terms of the evolution of snow cover throughout the hydrological season and in terms of their spatial variability in complex topography. This study could be considered a first attempt at using thermal inertia towards improved monitoring of the cryosphere. Limitations of and improvements to the proposed methods are also discussed.

This study may also help in defining the scientific requirements for new satellite missions targeting the cryosphere. We believe that a new class of Earth Observation missions with the ability to observe the Earth’s surface at high spatial and temporal resolution, with both day and night-time overpasses in both optical and thermal domain, is currently missing.

1. Introduction

Snow density is a key physical property of the snowpack (Bormann et al., 2013) and relevant to various facets of snow research, encompassing snow load estimation, avalanche prediction, energy balance, climate models and snow hydrology applications (e.g., Meløysund et al., 2007; Hirashima et al., 2009; Jonas et al., 2009; Koren et al., 1999; Livneh et al., 2010; Sturm et al., 2010; Bormann et al., 2013). In particular, the detection of snow density and snowmelt phases is valuable information in the Alpine environment, since it is well known that snow is a fundamental reservoir of freshwater in downstream valleys, especially in the mid-latitudes (Immerzeel et al., 2020). Knowing the spatial and temporal variability of snow density in mountainous regions could allow better modelling of the snow water equivalent, vital for managing freshwater resources under changing climate (e.g., McCreight and Small, 2014; Raleigh and Small, 2017).

Snow is a three-phase medium composed of ice, liquid water and air. Conceptually, it is possible to distinguish two fundamental periods during the snow season: accumulation and melt. The accumulation period features the interplay of snowfalls, generally characterized by dry and low-density snow, followed by compaction and metamorphism processes. The snowmelt period can be defined as the timeframe when warming, ripening and output processes occur within the snowpack, with rising liquid water content and increased snow density (Dingman, 2015; Arenson et al., 2015; Oke, 1987). Overall, snow density affects the thermal and mechanical properties of the snowpack. It is widely recognized that snow density shows a significant temporal and spatial variability in response to meteorological drivers (e.g., solar radiation), as well as topographic attributes (e.g., elevation and slope) and to overall geographic context (Meløysund et al., 2007; Jonas et al., 2009; Mizukami and Perica, 2008; Svoma, 2011; Onuchin and Burerina, 1996; Grünewald et al., 2010; Sturm et al., 2010; Lastrada et al., 2021; Valt et al., 2018). To date, spatial and temporal patterns of snow density are inferred using various methods, including field measurements, modelling and remotely sensed data (e.g., Broxton et al., 2019).

Remote sensing provides a unique opportunity to estimate snowpack properties in space and time by exploiting different spectral domains (König et al., 2001; Dozier and Painter, 2004). Specifically, extensive efforts for retrieving snow density were performed using both active (Shi and Dozier, 2000; Snehmani et al., 2010; Thakur et al., 2012) and passive microwave remote sensing, thanks to the ability of the radiation at longer wavelengths to propagate through the snowpack (Champollion et al., 2018; Lacroix et al., 2009; Lemmetyinen et al., 2016; Naderpour et al., 2017; Roy et al., 2017; Schwank et al., 2015; Schwank and Naderpour, 2018). However, it is still a great challenge to obtain accurate estimates of snow density from these remote sensing methods. Instead, optical and thermal data are traditionally used to estimate near-surface snow characteristics, rather than snow density. Numerous studies have demonstrated the ability to detect snow cover extent, grain size, surface albedo, liquid water content, light-absorbing particles, snow surface temperature and spectral emissivity (Bormann et al., 2018; Dozier and Painter, 2004; Green et al., 2002; Kokhanovsky et al., 2018; Painter et al., 2013; Skiles et al., 2018; Aubry-Wake et al., 2015, Hori et al., 2013, Bohn et al., 2022). Recently, Colombo et al., (2019), demonstrated the possibility of using optical and thermal data to compute thermal inertia and to estimate snowpack density.

Thermal inertia is defined as a measure of the medium admittance to temperature changes. It depends on density, thermal conductivity and specific heat of the material and it is expressed in J m^{-2} K^{-1} $s^{-0.5}$ units. Thermal inertia governs surface temperature variations and measures the medium thermal response to diurnal (or annual) heat flux variations (e.g., Carlson et al., 1981). Regarding snow surfaces, light penetration and heat fluxes can vary at daily and seasonal scales, according to snow conditions. The incident solar radiation that penetrates the snowpack is absorbed and scattered by snow grains within approximately the top ten to twenty centimetres, the depth at which the penetrating radiation extinction is almost 99% (Libois et al, 2013; Fukami et al, 1985; Zhong et al, 2017; Perovich, 2007; Järvinen et al, 2011; Kokhanovsky, 2022). Daily surface temperature variations propagate heat into the snowpack to a depth of approximately fifty centimetres (Oldroyd et al, 2013), although during the melting season, this depth can be even greater. Colombo et al. (2019) introduced a theoretical model to compute snow thermal inertia (Ps) and demonstrated the potential of the so-called apparent thermal inertia (APs) to detect snowmelt dynamics and the snow density of the snowpack. Unlike thermal inertia, APs can be estimated using remote sensing, typically starting from the knowledge of incoming radiation, shortwave albedo, and surface temperature difference between day and night (Price, 1980; Xue and Cracknell, 1995; Sobrino et al., 1998). Apparent thermal inertia has been successfully exploited in various applications, regarding surface planetary geology, urban heat island and soil moisture detection (e.g., Aït-Mesbah et al., 2015; Brenning et al., 2012; Putzig and Mellon, 2007; Wang et al., 2010, Short and Stuart 1982; Minacapilli et al., 2009, Maltese et al., 2013; Van Doninck et al., 2011, Murray and Verhoef 2007). However, for cryosphere monitoring, it is still in the early stages albeit with considerable potential. Indeed, as in the case of soil applications where thermal inertia is used to infer moisture content within the soil profile (e.g., Van Doninck et al., 2011, Nearing et al., 2012, Paruta et al., 2021), for snow applications, thermal inertia is expected to provide information on the snow density of the snowpack (Colombo et al., 2019).

To date, the possibility of mapping snow density at the catchment level in mountainous terrains using thermal inertia from spaceborne measurements is limited. Satellites providing optical and thermal data with high revisit time (e.g., MODIS/VIIRS) have low spatial resolution while those with high spatial resolution (e.g., Landsat) have low temporal resolution and do not provide regular night-time measurements. New perspectives can be provided by some of the upcoming satellite missions, such as the Copernicus Land Surface Temperature Monitoring (LSTM), the Surface Biology and Geology Thermal Infrared (SBG TIR) and the Thermal infraRed Imaging Satellite for High-resolution Natural resource Assessment (TRISHNA). The possibility of exploiting snow thermal inertia for snow density monitoring may indeed open new frontiers in the remote sensing of the cryosphere. To our knowledge, the only qualitative consideration of the spatial variability of the apparent thermal inertia of snow in hydrological basins has been deduced by Short and Stuart (1982) in the framework of the NASA Heat Capacity Mapping Mission.

In this context, we propose a novel approach to obtain thermal inertia and snow density maps from multitemporal Landsat-8 data, meteorological parameters and snow field measurements in Alpine catchments sited in the Western Italian Alps. Our rationale is that since changes in snow density occur continuously in the snowpack, spatial and temporal patterns of thermal inertia could theoretically reflect snow dynamics. Thermal inertia was empirically related to in situ manual measurements of snow density to demonstrate the possibility to monitor snow density at catchment level from optical and thermal observations. This study may be considered a first attempt at using the remote estimation of thermal inertia to understand the evolution of the snowpack and the snow density variability in complex topography, hence supporting improved monitoring of the cryosphere.

2. Material and methods

2.1 Study area, dataset and method overview

The study area is sited in the Aosta Valley in the Western Italian Alps (Figure 1). It includes four catchments, covering a total area of ~140 km^2 with a rather significant altitudinal gradient (1956 to 4119 m, asl), complex morphology and variable meteorological conditions.

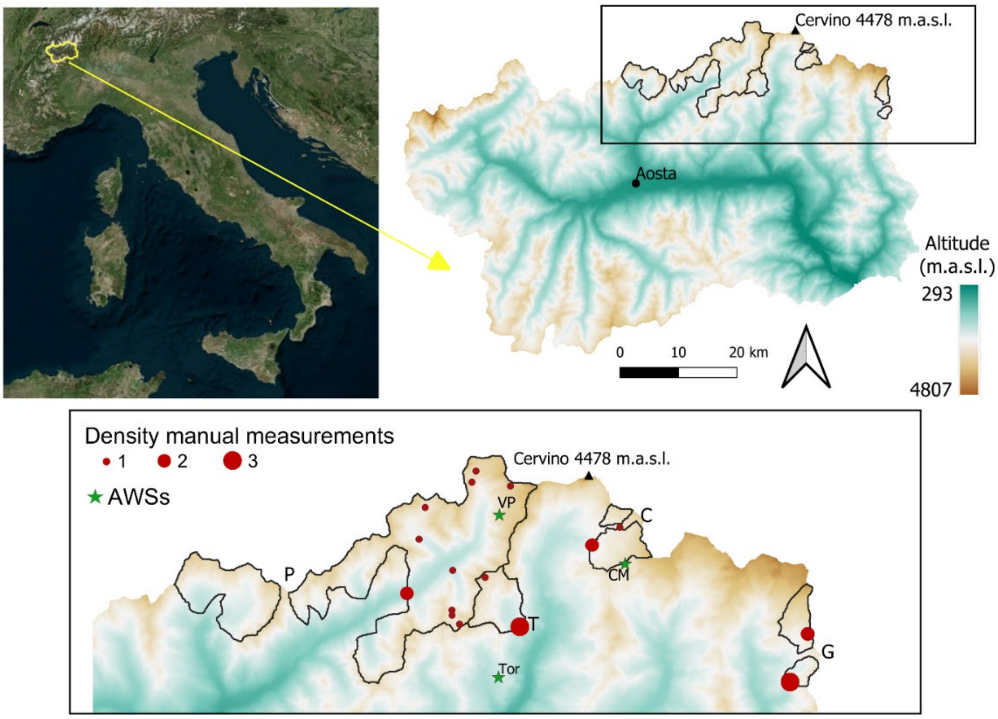

Figure 1: Investigated catchments (Valpelline, P; Gressoney, G; Cervinia, C and Val Tournenche, T) depicted on the Digital Elevation Model of the Aosta Valley. Red dots indicate the locations of in situ snow density measurements with dot size proportional to their abundance; green asterisks identify the positions of the Automatic Weather Stations (AWS) used for comparison purposes (Torgnon, Tor, Cime Bianche, CM and, Valpelline, VP stations).

All basins are mainly located above the treeline (approximately 2000 m asl): forest cover is absent or negligible in all basins. Slopes steeper than 60° occupy on average less than 5% of the four investigated catchments. Maximum snow depth at the end of the accumulation season (April-May) can range from 1.5-2.5 m at lower elevations (2000 m asl) to as much as 4-6 m at the highest elevations (4200 m asl, Avanzi et al 2021). Mean winter air and dew point temperature at 2000 m asl (Tor AWS, see Figure 1) are -2.8 ± 4.6 °C and -10.6 ± 5.27 °C, respectively (daily mean ± daily std.dev.) and -8.30 ± 4.85 °C and -15.4 ± 5.92 °C, respectively at 3100 m asl (CM AWS, see Figure 1).

To understand the snowpack evolution from accumulation to melting, we selected different days representing different snow hydrological conditions for which a simultaneous combination of snow density in situ measurements and cloud-free satellite images were available; the investigated period covers six days from the 2014/2015 to 2019/2020 hydrological seasons.

For this study, we exploited six Landsat 8 OLI (Operational Land Imager) and TIRS (Thermal Infrared Sensor) Collection 2 images acquired between January and May (Table 1) at 11.30 a.m. Satellite data were gathered from the USGS website and used to compute the surface albedo (α, dimensionless) and to exploit the Collection 2 surface temperature product (Ts, K).

Meteorological data provided by fifteen Automatic Weather Stations (AWS) distributed outside and within the catchments, were used to obtain incoming shortwave radiation (SW_{in}, W m^{-2}) and night-time dew point temperature (Td, K) maps. We also used three additional stations, namely Valpelline (VP, 3100 m), Cime Bianche (CM, 3160 m) and Torgnon (Tor, 2150 m), equipped with CNR4 (Kipp and Zonen) net radiometers, for validation purposes (Figure 1).

A total of twenty-six snow density measurements (ρ, kg m^{-3}) were manually collected at different sites and on different days during snow water equivalent campaigns devoted to water resource monitoring programs run by regional authorities and hydropower companies. The location of in situ snow measurements are shown in Figure 1. Data were sampled in snow pits with horizontal snow samplings at fixed depths. Each snow pit falls within a different Landsat pixel. In this study, we considered both the snow density of the upper 30 cm and the bulk density of the whole snowpack. Table 1 reports the main snow characteristics derived from field surveys sampled in correspondence with the Landsat 8 overpasses.

Table 1 Landsat 8 images used in this study and main information on snow characteristics from field measurements.

Landsat images	**Snow density range 30cm (kg m^{-3})**	**Snow density range snowpack** (kg m^{-3})	**Snow depth range (cm)**	**Abundance of field samples (n°)**
10/05/2015	415-615	415-615	96-320	3
13/04/2017	300-485	314-505	70-390	10
29/01/2019	230-270	322-364	130-220	2
16/01/2020	260-330	297-335	65-180	5
04/03/2020	173-300	302-390	95-155	3
05/04/2020	313-455	408-410	53-142	3

This combination of input data allowed us to design an innovative approach to compute thermal inertia at catchment level and to infer snow density by developing an empirical regression model between apparent thermal inertia and surface/bulk snow density. Figure 2 shows an overview of the approach workflow, which is fully explained in the next sections.

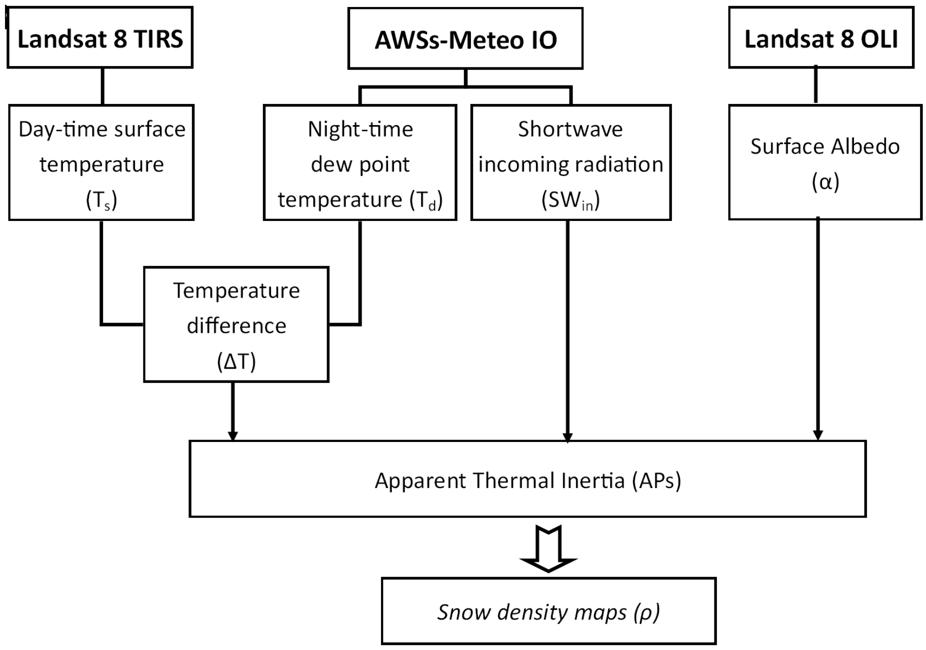

Figure 2: Overview of the approach used to generate snow density maps.

2.3 Retrieval of snow albedo and temperature from Landsat data

Snow surface albedo was computed for all the catchments from the Landsat 8 OLI images. To retrieve surface reflectance from Top of Atmosphere (TOA) radiance data, we used the ATCOR4 (Atmospheric and Topographic CORrection) software (Richter and Schläpfer, 2015), by defining an ad-hoc configuration for Landsat imagery. This code corrects imagery for atmospheric and adjacency effects and to normalise the impact of topography, which might be significant in rugged terrain. For this purpose, we incorporated an accurate Digital Elevation Model (DEM) with 10 m spatial resolution. Shortwave surface albedo was computed without considering the anisotropy of the snow surface reflectance. The narrow-to-broadband conversion was conducted starting from reflectance data by using standard formulation developed for Landsat 5/7 data (Liang et al, 2001) and previously exploited for snow applications with OLI images (Naegeli, et al., 2017; Ren et al., 2021):

$$\alpha = 0.356b_2 + 0.130b_4 + 0.373b_5 + 0.085b_6 + 0.072b_7 - 0.0018 \quad [-] \qquad (1)$$

where b_n represents the spectral channel number of Landsat 8 reflectance data [i.e., b_2 (0.452-0.512 μm), b_4 (0.636-0.673 μm); b_5 (0.851-0.879 μm), b_6 (1.566-1.651 μm), b_7 (2.107-2.294 μm)].

Albedo values higher than 1 were filtered out in the following analyses. These pixels accounted for 1% of the scene in May 2015 and 4% in January 2019 and 2020.

Landsat 8 day-time surface temperatures (Ts) used in this study correspond to the standard surface temperature product, obtained by the Landsat Single-Channel v1.3.0 algorithm.

Landsat shortwave broadband albedo and daily surface temperature maps were compared with data recorded by AWS stations and their quality was evaluated in terms of coefficient of determination (R^2) and root-mean-square error (RMSE).

2.4 Generation of the shortwave incoming radiation and night-time surface temperature maps

Meteorological input data at a spatial resolution comparable with OLI data, namely air temperature (Ta), relative humidity (RH) and incoming shortwave radiation (SW_{in}) were produced with the meteorological pre-processing library MeteoIO (Bavay and Egger, 2014).

The MeteoIO numerical library retrieves, filters and spatially interpolates meteorological data coming from nearby AWS stations belonging to the regional weather network. For each catchment, five to seven stations were used. All the meteorological variables were spatially interpolated with an inverse distance-weighting algorithm. Regarding Ta and RH, a lapse rate with elevation was also applied (Bavay and Egger, 2014). All these maps have been computed at different times of day and night (i.e., at a 1-hour step) in correspondence with the Landsat acquisition dates.

Daily mean SW_{in} maps in the 305-2800 nm spectral range were obtained by averaging all hourly radiation values greater than 20 W m^{-2}, as suggested by Wang and Liang (2009).

In the absence of night surface temperatures at the desired spatial scale, we tested the option of approximating night-time snow surface temperature with dew point temperature (Td), as proposed by Raleigh et al. (2013). Td is the temperature to which air needs to be cooled to become saturated with water vapour and it indicates how much moisture is in the air:

$$T_d = \frac{c\left[ln\,(RH) + \frac{bT_a}{c+T_a}\right]}{b - ln\,(RH) - \frac{bT_a}{c+T_a}} \quad [°C] \qquad (2)$$

where, RH and T_a are the relative humidity and air temperature at different time of the night, respectively. The empirical coefficients b and c were set as indicated in Raleigh et al. (2013).

Andreas (1986), firstly proposed the use of the dew point temperature for approximating snow surface temperature. The physical reason for this approximation is that snow cover is a saturated surface, such that the vapour pressure of air close to the surface equals the saturation vapour pressure. Air reaches saturation at Td, and the saturation vapour pressure is a function of Ts alone; thus, Td close to the snow surface is in equilibrium with Ts. Raleigh et al. (2013) demonstrated that Td is a reliable approximation of Ts, especially during night-time and at locations and times where turbulent mixing occurs frequently, such as in Alpine areas.

To understand the time at which Td best approximates surface temperature, we evaluated the robustness of the relationship between Td and surface temperature at different hours of the night, by performing a correlation analysis starting from the data recorded at the three AWS. We considered all the 2017-2020 hydrological seasons and we computed R^2, mean bias and RMSE. Multitemporal maps of night-time Td at the selected time were finally produced using Eq. 2.

2.5 *Δ*T computation

The difference in surface temperatures was computed by combining night-time Td, derived from meteorological modelling, with daily surface temperature derived from Landsat TIRS data ($\Delta \mathrm{T} = \mathrm{Ts} - \mathrm{Td}$). In some cases, we found negative ΔT values (i.e., day-time temperature was lower than night-time). In these cases, the pixels corresponding to these specific conditions were discarded in the rest of the analyses. Overall, these pixels accounted for about 1% of all the images, except for 2019 January 29th, where we found that about 50% of the pixels had negative ΔT values.

2.6 APs and snow density maps

Thermal inertia APs was computed using the solution of the one-dimensional thermal diffusion equation as suggested by Xue and Cracknell (1995) and used in Colombo et al. (2019) for snow applications:

$$APs = \frac{(1-\alpha)\, SW_{in}\, A_1[\cos(\omega t_2 - \delta_1)\ - \cos(\omega t_1 - \delta_1)]}{\Delta T_{(t2-t1)}\sqrt{\omega}\sqrt{1+\frac{1}{b}+\frac{1}{2b^2}}} \qquad [Jm^{-2}K^{-1}s^{-0.5}] \quad (3)$$

where,

α = shortwave albedo $[-]$;

SW_{in} = incoming shortwave radiation $[\mathrm{W\ m^{-2}}]$ averaged in day-time hours;

A_1 and b = coefficients of first-order approximation of the Fourier series, which depends on latitude and solar declination and azimuth, computed according to Xue and Cracknell (1995);

ω = Earth's rotation angular velocity $[7.2921150\ x\ 10^{-5}\ \mathrm{rad\ s^{-1}}]$;

δ_1 = phase difference between surface temperature and shortwave incoming radiation, $[\mathrm{rad}]$. $\delta_1 = \omega t_{max}$=3.794, with t_{max}=14:30

ΔT = surface temperature difference between the night-time and the day-time temperatures measured at times t_1 (04:00) and t_2 (11:30), respectively $[\mathrm{K}]$.

Besides ω, b and δ_1, all the other parameters of Eq. 3 change in space and time. The A_1 values range from 0.15 to 0.48, while the b parameter value is equal to 3.298. APs maps were computed for all snow-covered pixels, except for those discarded for anomalous (negative) ΔT and albedo values higher than 1 (NoData). Maps of snow cover were obtained by applying a threshold on the Normalised Difference Snow Index (NDSI) (Hall et al., 1995). A NDSI threshold higher than 0.6 was selected by visual inspection of the histogram distribution and then applied to each image to define snow-covered and snow-free pixel masks (NoSnow). Although a threshold of 0.4 is considered standard for generating snow cover maps, its spatial/temporal representativeness at local scale is debated and different values may be used (Härer et al., 2018).

The relationship between APs maps and manually measured surface and bulk snow density was finally derived by a regression analysis. We averaged AP values within 3x3 pixels centred on corresponding snow density field measurements, to reduce systematic errors due to geolocation uncertainties. The relationship between thermal inertia and snow density was established using inverse ordinary least squares (OLS) regression techniques and evaluated in terms of R^2 and RMSE. Using the OLS technique, we calibrated the so-called "inverse form" of the empirical relationship. In particular, we employed the snow density variable as predictor X and thermal inertia as the dependent variable Y to estimate the OLS coefficients. The validation of the OLS model was performed with the K-fold approach splitting the dataset into 8 subsets. Then the model was fit using 7 subsets, as the training set and the validation was conducted using the omitted subset. The performances of the model were evaluated in terms of cross-validated coefficient of determination (R^2_{CV}) and cross-validated root mean square error ($RMSE_{CV}$).

The developed empirical regression model was exploited to produce multitemporal maps of surface snow density in the four catchments. APs and snow density maps were mainly interpreted by considering the accumulation (January) and melting periods (May) and considering their spatial patterns and meteorological conditions. We also discussed the spring season (i.e., March and April), where both conditions may coexist and snow thermal inertia and density can exhibit high spatial variability.

3. Results and discussion

3.1 Shortwave incoming radiation maps

The SW_{in} maps generated with MeteoIO on 16 January 2020 and 10 May 2015 and the corresponding frequency histograms of the investigated catchments are shown in Figure 3. As expected, the incoming radiation shows variability over time, with low SW_{in} values during the winter months in the accumulation period (shorter duration of daily solar illumination) and maximum values reached in spring during the melting season. Besides the seasonal evolution of incoming radiation, Figure 3 also shows the effect of aspect: south-exposed slopes receive a higher amount of solar radiation compared to north-exposed ones.

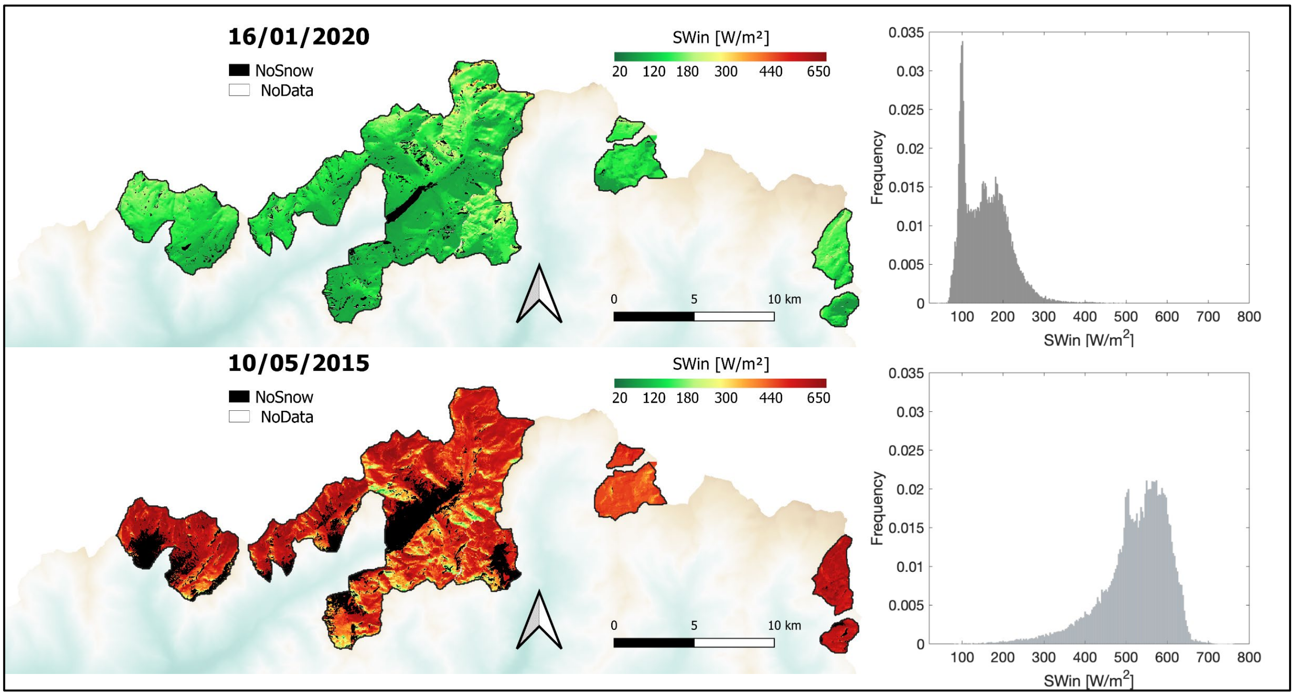

Figure 3: Spatial and temporal variability of solar irradiance during the accumulation period (January) and the melting phase (May). Black (i.e., NoSnow) represents no snow pixels, while white ones (i.e., NoData) have no values. The histograms describe the value distribution (the frequency is expressed from 0 to 1) during these two periods, for all the investigated catchments.

Each of the selected dates were characterized by clear sky throughout the day, and during March and April, we found consistent incoming solar radiation values, coherent with AWS measurements.

3.2 Spatial and temporal variability of snow albedo

The snow albedo maps and related histograms for the two periods are shown in Figure 4.

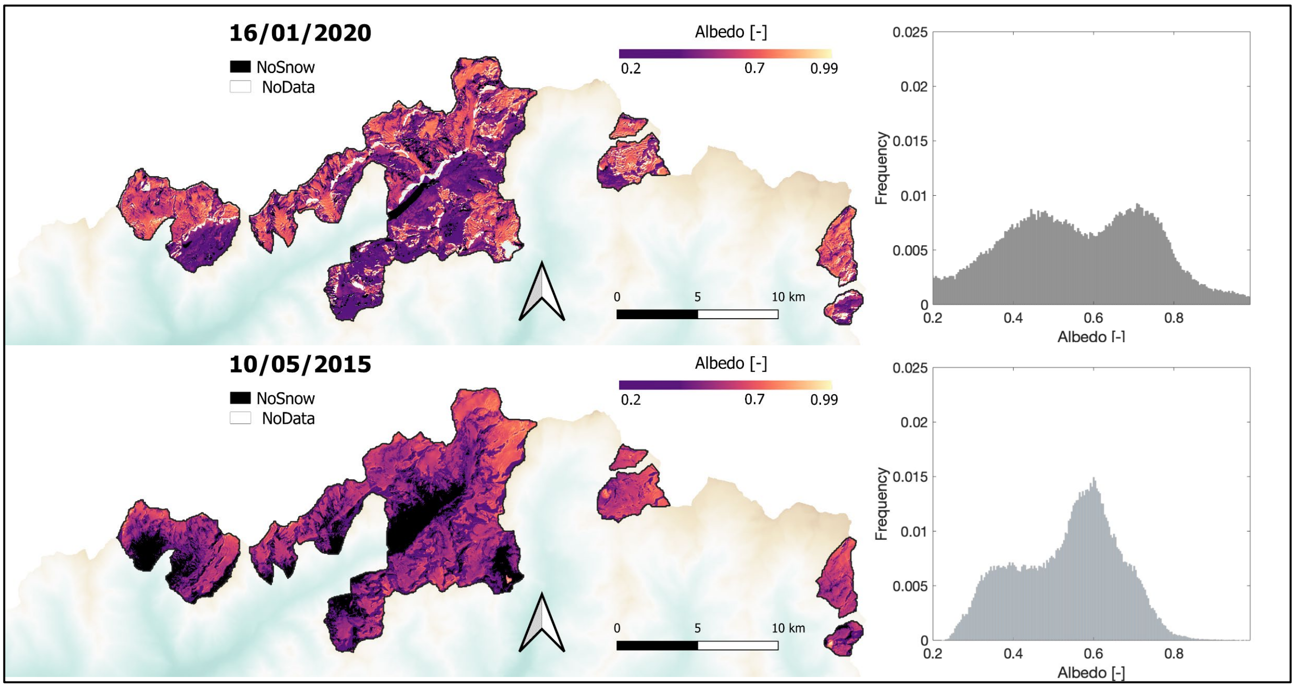

Figure 4: Spatial variability of snow surface albedo during the accumulation period (January) and the melting phase (May). Black represents no snow pixels, while white ones have no albedo values. The histograms describe the values distribution during these two periods for all the investigated catchments (the frequency is expressed from 0 to 1).

As expected, we observed that albedo decreases from January to May with histograms showing a distribution that is the consequence of local snow conditions during accumulation and melting seasons.

During winter, the highest albedo values are related to fresh snow and continuous snowfalls that typically occur at higher elevation in the study area. Low albedo values may also occur: these can be associated with either old snow or dirty snow at the bottom of the valley, where snow conditions might be also affected by human activity.

Average albedo values in May are lower compared to the winter season due to snow ageing, potential light absorbing particles and changes in grain size (Painter et al., 2013; Di Mauro et al., 2019; Hadley and Kirchstetter, 2012, Libois et al, 2013; Fukami et al, 1985; Kokhanovsky, et al., 2021). Over the season (i.e., from March to April), we encountered intermediate and variable albedo values, with high spatial variability within the catchments. The number of pixels discarded due to anomalous surface albedo values was very small. These pixels correspond mainly to fresh snow and the anomalous values are probably due to defective atmospheric/topographic correction and the empirical weighting parameters used in narrow- to broad-band conversion.

Overall, our interpretation of albedo might suffer from having considered snow reflectance as Lambertian, while the anisotropy of snow reflectance might also be responsible for albedo variations across the scene (e.g., variable slopes, aspects and snow impurities) (Dumont et al., 2010). The shadowing effect also introduces further uncertainties in snow albedo estimation. Figure 4 shows a bimodal behaviour, where low albedo values are related to snow surfaces sited on terrain which was mainly shadowed during the satellite overpass. Although cast shadows were considered in the atmospheric correction process, the results highlight the need to improve terrain-based shadow correction for future applications. This applies particularly to images acquired when solar irradiance is minimal and shadows are maximal, such as the January data in this study.

We found a coefficient of determination equal to 0.41 when comparing albedo estimates with albedo measurements in AWSs located at CM, VP and Tor sites (Figure 5). The scattering found in this comparison could be explained by the heterogeneity of snow surface properties within the spatial resolution of Landsat-8 data and considering that the snow albedo was computed without taking into account the snow anisotropy. The largest errors are identified for fresh snow conditions (e.g., in January) and they are conceivably related to marked anisotropy effects for increasing illumination angles (Dumont et al. 2010).

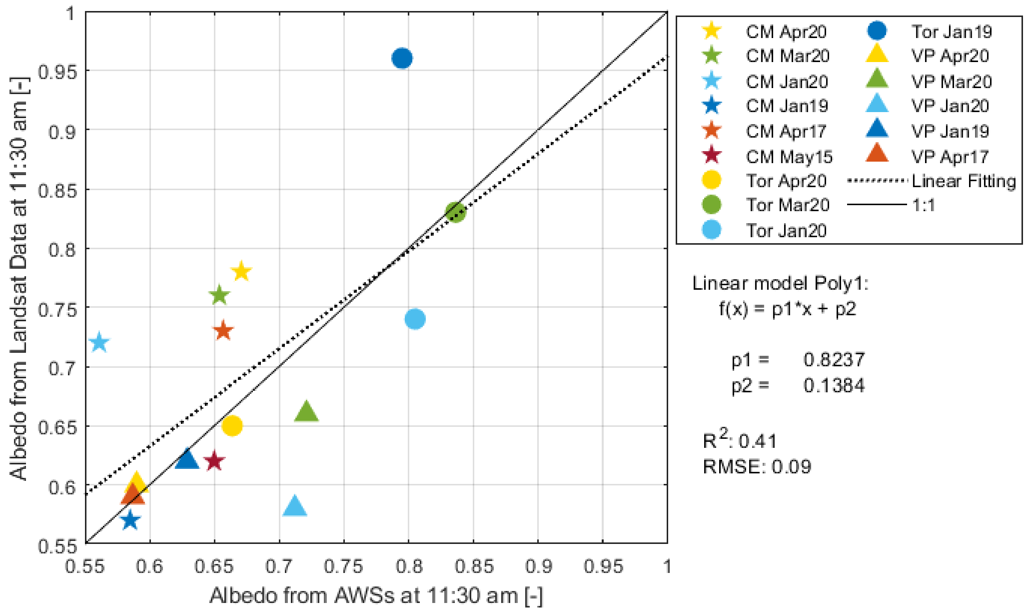

Figure 5 Comparison between surface albedo derived from Landsat data and albedo recorded at the AWs

In summary, the comparisons of AWS data across seasons and sites might be compromised by changes in snow albedo due to snow properties and sun-target-viewing geometries, the latter being particularly variable in this complex topography. Similar broadband albedo comparison conducted in more homogeneous areas (e.g., the Greenland Ice Sheet) resulted in fact in a greater consistency between satellite retrievals and AWS data (Kokhanovsky et al. 2019).

3.3 Spatial and temporal variability of snow ΔT

Before computing the surface temperature difference maps, we evaluated the quality of the day-time temperatures provided by Landsat TIR (Figure 6) and the strength of the correlation between dew point temperature and surface temperature at night (Figure 7).

Despite a slight underestimation, Figure 6 shows a good correspondence between snow temperature measured with the AWS and satellite temperature (R^2 = 0.87; RMSE = 2.71 K), suggesting the high quality of the Landsat TIR data for snow surfaces. The deviation of a single measurement (i.e., CM, May 2015) from the 1:1 line is likely associated with snow patches caused by wind effects, causing a mixture in Landsat pixels.

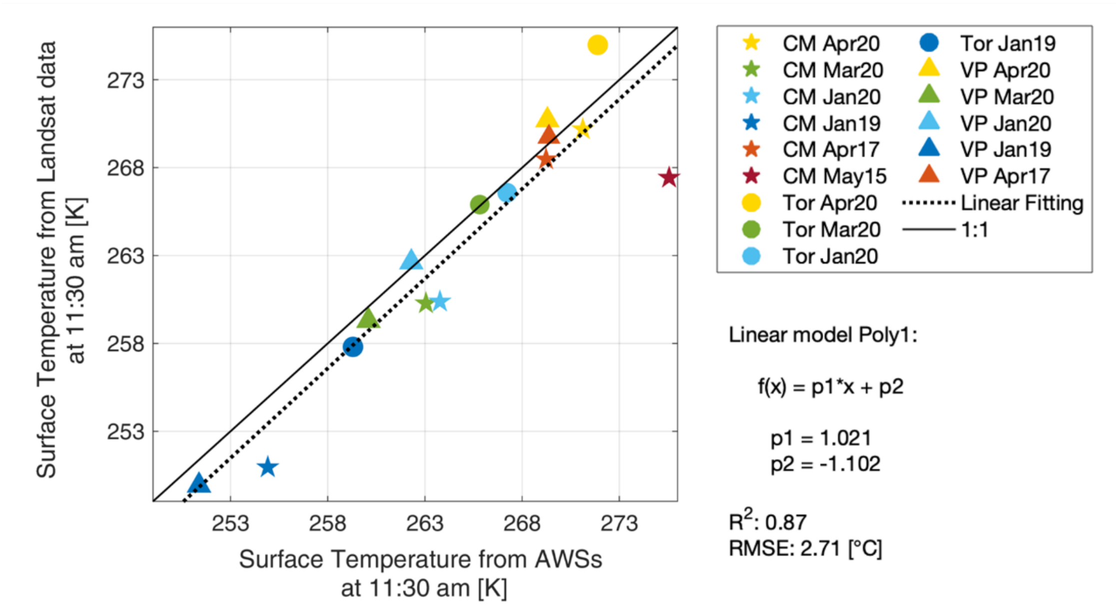

Figure 6: Comparison between snow surface temperature and Landsat snow surface temperature at Cime Bianche (CM), Torgnon (Tor) and Valpelline (VP) AWSs. The closest pixel to the station was taken into account.

The Td that best approximates night-time temperature was that measured at 04.00 a.m. We found a significant linear relationship between surface temperature and Td at 04.00 for all the AWSs (e.g., $R^2 = 0.69$ and RMSE = 3.4 K at the Torgnon site, data not shown). Figure 7 shows the agreement between the night-time Td and the corresponding surface temperature recorded at the three AWS stations for the six selected days.

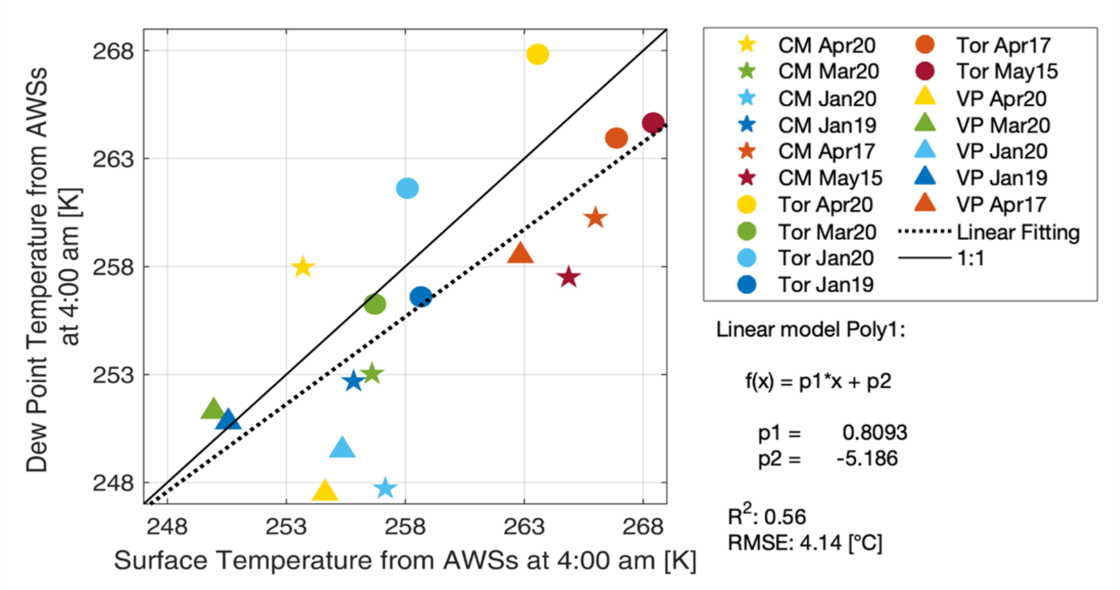

Figure 7: Comparison between night-time dew point temperature and surface temperature recorded at the AWs

Figure 7 shows a large scatter between dew point and snow surface temperature, with results worse than those obtained with Landsat data. According to Raleigh et al. (2013), Td approximates Ts best when there is high wind shear (i.e., unstable boundary conditions) and when there is no vapour pressure gradient between the near-surface atmosphere and the snow surface (i.e., no sublimation or condensation). Although these conditions frequently occur in the investigated catchments, the discrepancy in Figure 7 could be due to a local variability of near-surface atmospheric stability, indicating the weakness in using the dew point temperature instead of the surface temperature. Although the dew point temperature is not the surface temperature and is not exactly computed at the time when the minimum surface temperature occurs (i.e., around 06.00 a.m. in these areas), we believe that Td is a useful approximation and provides an indication of the nigh-time minimum temperature to be used to generate the ΔT maps. From Figure 7, we can also infer that errors in ΔT may vary in space, with different impact on the APs maps. For example, in April 2020, we can expect APs overestimation at the Torgnon site located at a lower elevation and underestimation of APs at Cime Bianche, sited at a higher elevation. A preliminary Monte Carlo analysis (10000 samples) was performed to propagate day/night temperature uncertainties on ΔT, considering the range of variability in our data and the RMSE obtained in Figures 6 and 7. Under this condition, we found a ΔT uncertainty of 51.4 % and a standard deviation of 4.7 K. However, these errors result from the use of dew point temperature and we are confident that by using satellite data, performance will improve.

The spatial and temporal patterns of ΔT in the accumulation and melting periods and the related histograms in the investigated catchments are shown in Figure 8.

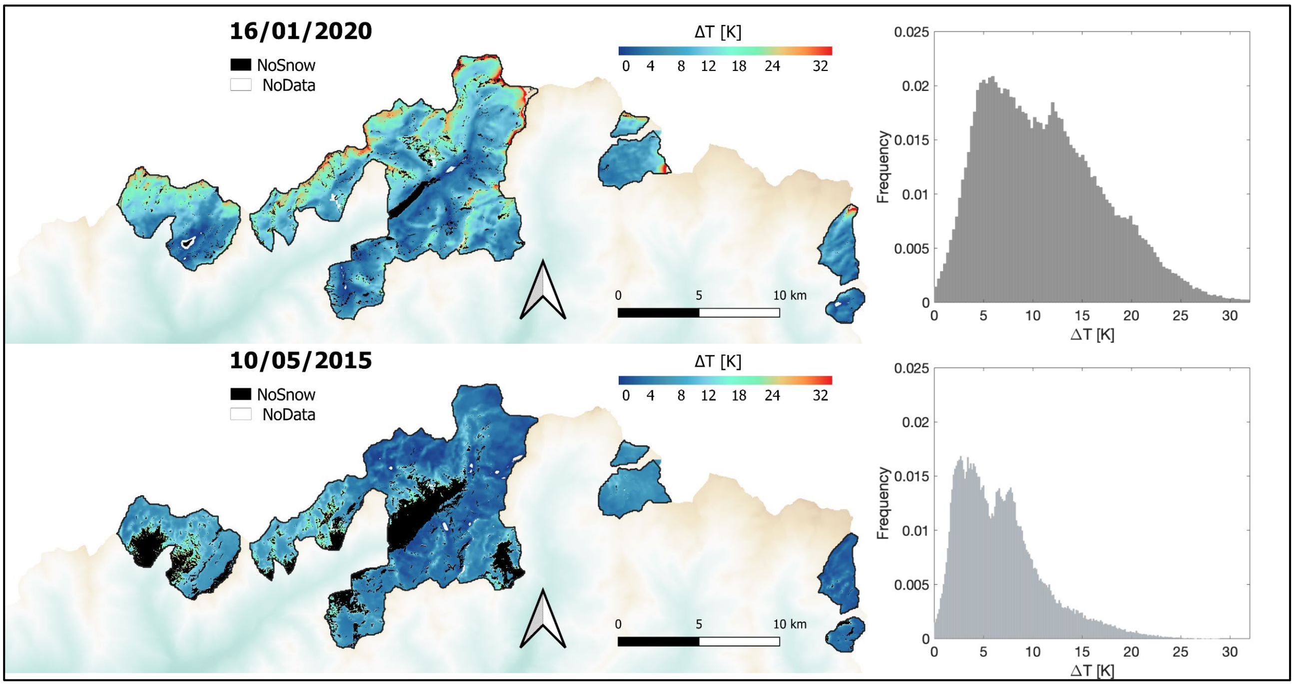

Figure 8: Spatial and temporal variability of snow surface temperature difference during the accumulation period (January) and the melting phase (May). Black represents no snow pixels, while white ones have no ΔT values. The histograms underline the values distribution during these two periods for all the investigated catchments (the frequency is expressed from 0 to 1).

As expected, surface temperature differences decrease over time and values are coherent with those computed using the AWs (data not shown). This result is also consistent with those achieved in previous investigations (e.g., Oesch et al., 2002).

The observed ΔT spatial patterns are most likely to be the result of the complex interplay between the variability in small-scale meteorological drivers and topographic factors, such as slope and aspect. For example, it is possible to find local snow melting in winter or abundant snowfalls with low temperatures in spring. For this reason, and considering the uncertainty in the night-time temperature maps, the interpretation of ΔT is not straightforward.

Overall, ΔT values are higher in January than in May. Snow temperatures are limited by 0 °C and this explain ΔT decreasing through the season. In January, ΔT shows a higher spatial variability with values that reach up to 30 K, in some cases. The highest values seem to occur for fresh snow along the ridges, which are the first to be illuminated in the early morning. A considerable dependency on altitude and aspects can be also noted. For example, at higher altitudes, where we encounter fresh snow, the ΔT is generally higher. Spatial variability is also related to snow exposure and shadowed slopes during the satellite overpasses. These are, in general, north-facing slopes and they exhibit lower ΔT since they have received less solar radiation.

Besides morphological effects, the local meteorological conditions during the night-day transition affect the surface temperature differences. According to the AWS data, most of the selected dates were characterized by clear sky conditions, both during the night (i.e., negative radiation balance and strong radiative cooling) and during the day (i.e., positive radiation balance). These are ideal conditions for thermal inertia estimation. However Pratt and Ellyett (1979) showed that the reliability of APs estimation as a function of ΔT is of reduced significance when ΔT tends to 0. In this study, we found negative and small ΔT values, which may be the result of local night-day dynamics. For example, January 29th, 2019 was the only night with overcast conditions (high incoming longwave radiation ~ 220 W m^{-2}, and high relative humidity, ~ 85%, and thus low radiative cooling), cloud cover decrease at sunrise, and clear sky conditions in the morning (inferred from the daily course of shortwave radiation). This specific behaviour (i.e., night-day transition from overcast to clear sky) reduced the surface ΔT to a small and negative values and introduced uncertainty to the estimation of thermal inertia and snow density. Therefore, we discarded numerous anomalous pixels for

January 2019. The APs values obtained at this time were slightly higher than those found in January 2020. From the perspective of space remote sensing, we highlight here that particular attention should be paid when night-time satellite acquisitions collected on cloudy nights are used to compute thermal inertia. For satellite applications this points to the need for a backup solution, also based on the dew point temperature, when images are affected by clouds. Small ΔT values may also appear in the melting season, related to patchy snow, heterogeneous pixels, freezing processes, presence of liquid water content and cloudy conditions. Overall, the snow surface temperature difference depends on the two selected instantaneous measurement times, meteorological conditions and heat exchanges occurring in the selected timeframe.

3.4 Thermal inertia maps and snow density retrieval

The spatial and temporal behaviour of APs with the corresponding histograms is shown in Figure 9.

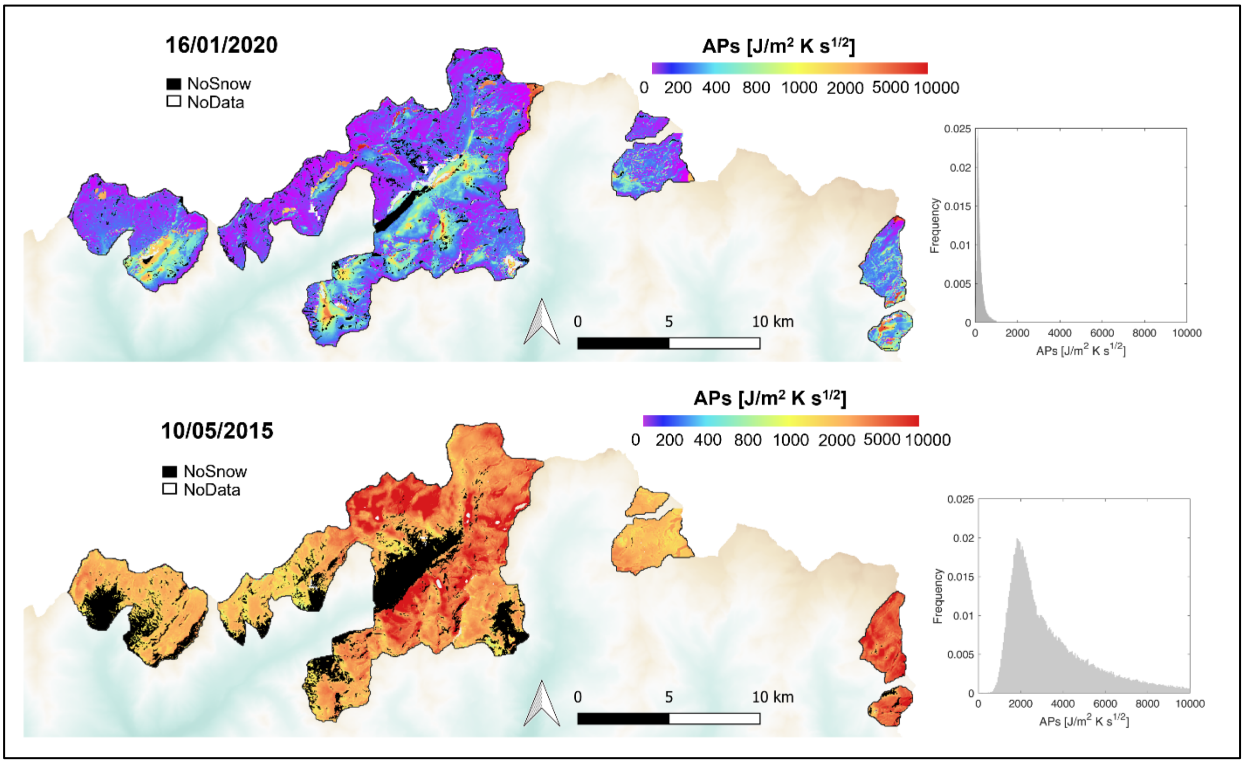

Figure 9: Spatial and temporal variability of snow thermal inertia during the accumulation period (January) and the melting phase (May). Black represents no snow pixels, while white ones have no APs values. The histograms underline the values distribution during these two periods for all the investigated catchments (the frequency is expressed from 0 to 1).

During January, APs show a low spatial variability, with mean, median and mode values of 220, 170 and 80 J m^{-2} K^{-1} $s^{-0.5}$, respectively. Greater spatial variability and higher APs values were found in May, where snow metamorphism quickly occurs and the appearance of liquid water content on the surface of the snow can increase apparent thermal inertia (2970, 2660 and 1840 J m^{-2} K^{-1} $s^{-0.5}$ for mean, median and mode, respectively). We can say, then, that lower APs values are characteristic of the accumulation period, while the highest values are typical of the end of the melting period during the output phase. During March and April, intermediate values of APs ranging from 500 to 1500 J m^{-2} K^{-1} $s^{-0.5}$ can be generally observed, indicating the transition between accumulation and snowmelt processes. In the meltwater output phase the APs values increase. Higher APs values are often associated with uncertain ΔT estimates and, as a whole, the range between 0 - 4000 J m^{-2} K^{-1} $s^{-0.5}$ represents the most appropriate interval to exploit for snow density applications.

Figure 10 shows the variability of APs over time, according to altitude, aspect, and slope. In the accumulation period, APs values remain within a narrow range of variability and they are not related to the spatial distribution of the topographic parameters. APs values recorded in January 2019 are higher than in January 2020 due to the particular night-time conditions. With the beginning of the snowmelt, we can observe that the variability of APs is sometimes related to the topographic parameters. Higher APs values can be found, for example, at a lower elevation and on southern and steep slopes, indicating areas where melting may occur or where snow accumulation does not take place. This is consistent with the pioneering observations of Short and Stuart (1982) who argued that higher values of apparent thermal inertia might define the extent of melting snow at the lowest elevations, while medium to low values are likely to represent drier, colder snow at the highest elevations.

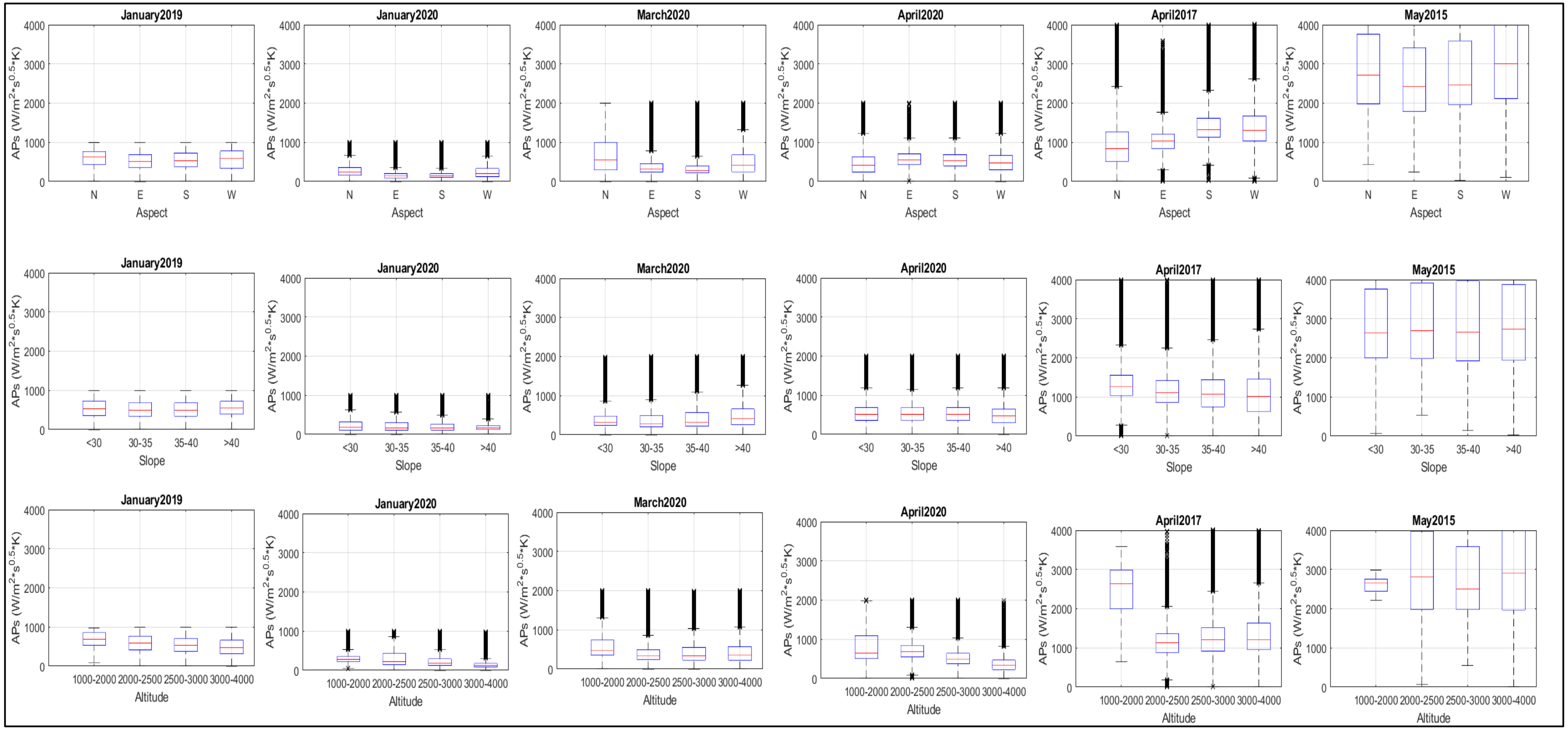

Figure 10. Box plot of the APs as a function of elevation, aspect and slope classes for all the analysed dates. The central mark indicates the median, while the bottom and top edges of the box indicate the 25th and 75th percentiles, respectively. The whiskers expand to the most extreme data points not considered outliers. Outliers are plotted individually using the '+' symbol.

To examine the snow APs values in a broader context, we checked the behaviour of other surfaces in May and we found values around 12400 J $m^{-2}K^{-1}s^{-0.5}$ for dam lakes and around 1200 and 1600 J $m^{-2}K^{-1}s^{-0.5}$ for rocks and alpine prairies, respectively. In summary, we showed for the first time that snow APs spatial and temporal distribution can change during the season and in different years, covering a wide range of values that can be exploited for snow monitoring. APs maps resulted consistent with the APs estimated from AWS data (R^2 = 0.74, data not shown).

A significant nonlinear relationship between APs and manually measured snow density was found, considering both the upper layer of 30 cm (R^2 = 0.65, Figure 11a) and bulk values of the whole snowpack (R^2 = 0.64, Figure 11b). Despite the uncertainty of the model, we can reasonably state that APs increases with snow density, as Colombo et al (2019) found using modelled data.

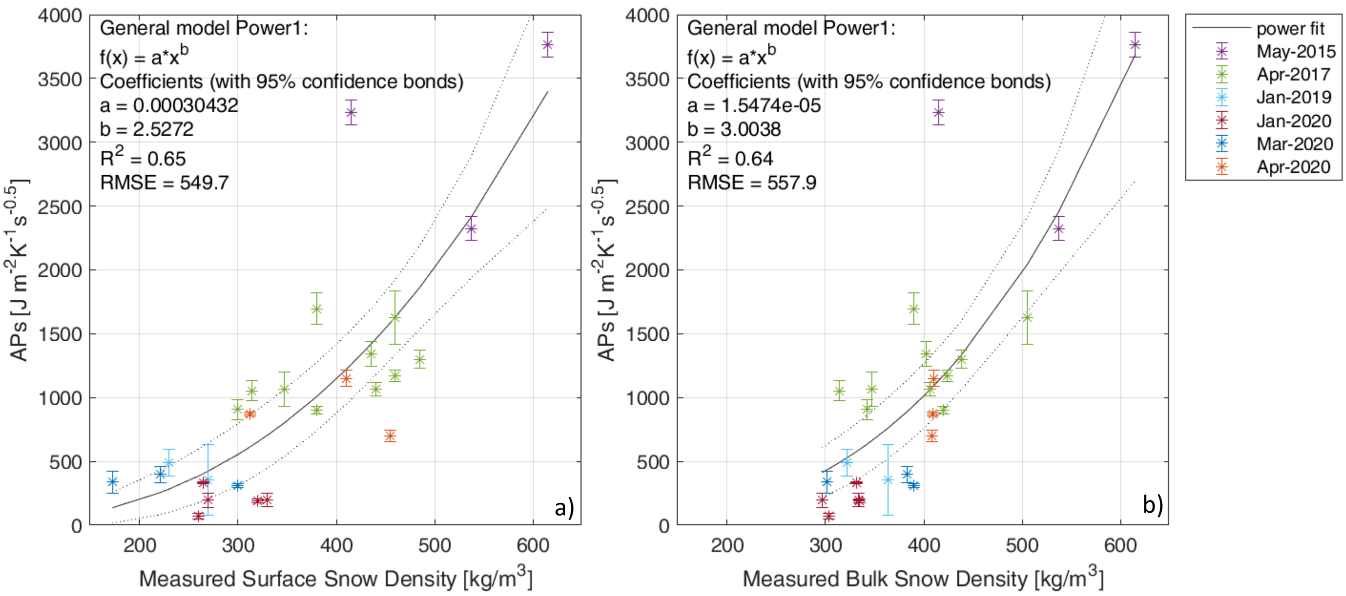

Figure 11: Relationship between APs and surface snow density (upper 30cm, a) and with bulk snow density, b). Colours indicate the different dates. Dotted lines indicate the confidence interval of the model. The error bars represent the standard deviation obtained averaging APs values in the neighbourhood of the density measurements.

Figure 12a shows the agreement between modelled snow density (Eq. 4) and measured snow density using the K-fold cross-validation. The model allows the estimation of snow density with R^2_{CV} and $RMSE_{CV}$ of 0.59 and 82 $\mathrm{kg\ m^{-3}}$, respectively.

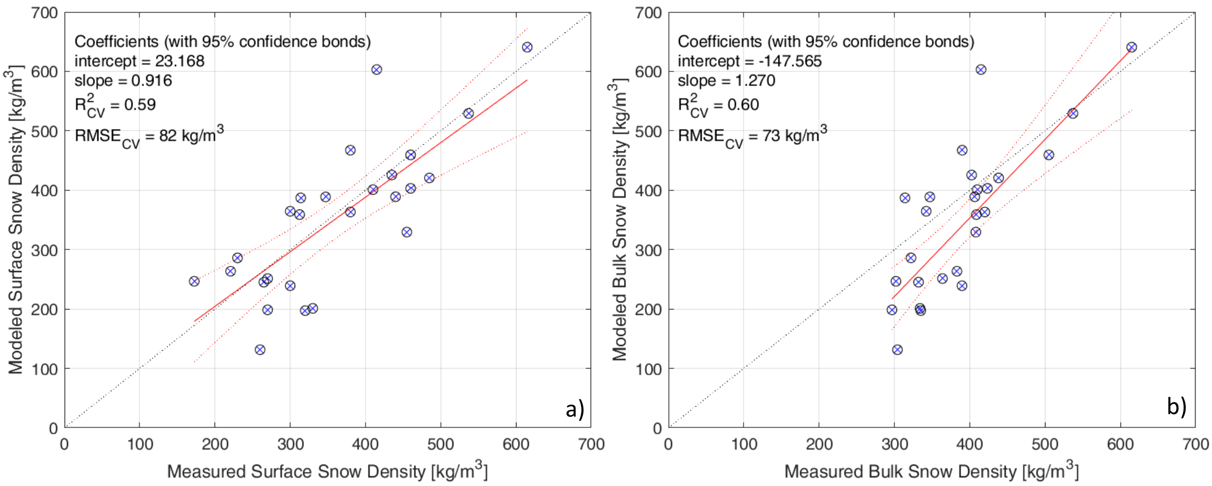

Figure 12 Comparison of the predicted and measured surface snow density (a) and bulk snow density (b)

The same analysis, considering the bulk snow density of the snowpack, provided a R^2_{CV} = 0.60 and a $RMSE_{CV}$ = 73 $\mathrm{kg\ m^{-3}}$, indicating the robustness of the approach (Figure 12b). Overall, surface snow density and bulk snow density were highly linearly correlated (R^2 = 0.75, data not shown).

Surface snow density maps were therefore computed by inverting the regression model shown in Figure 11a, according to the following equation:

$$\rho = \left(\frac{APs}{0.0003044}\right)^{\frac{1}{2.527}} \qquad \left[\frac{kg}{m^3}\right] \qquad (4)$$

Figure 13 shows the snow density maps obtained for January and May and the corresponding histograms. Basically, the regression coefficients we found should be understood as valid only within the snow density range measured in the present study, so that for Figure 13 we mapped snow density only in the 0 - 650 $\mathrm{kg\ m^{-3}}$ range.

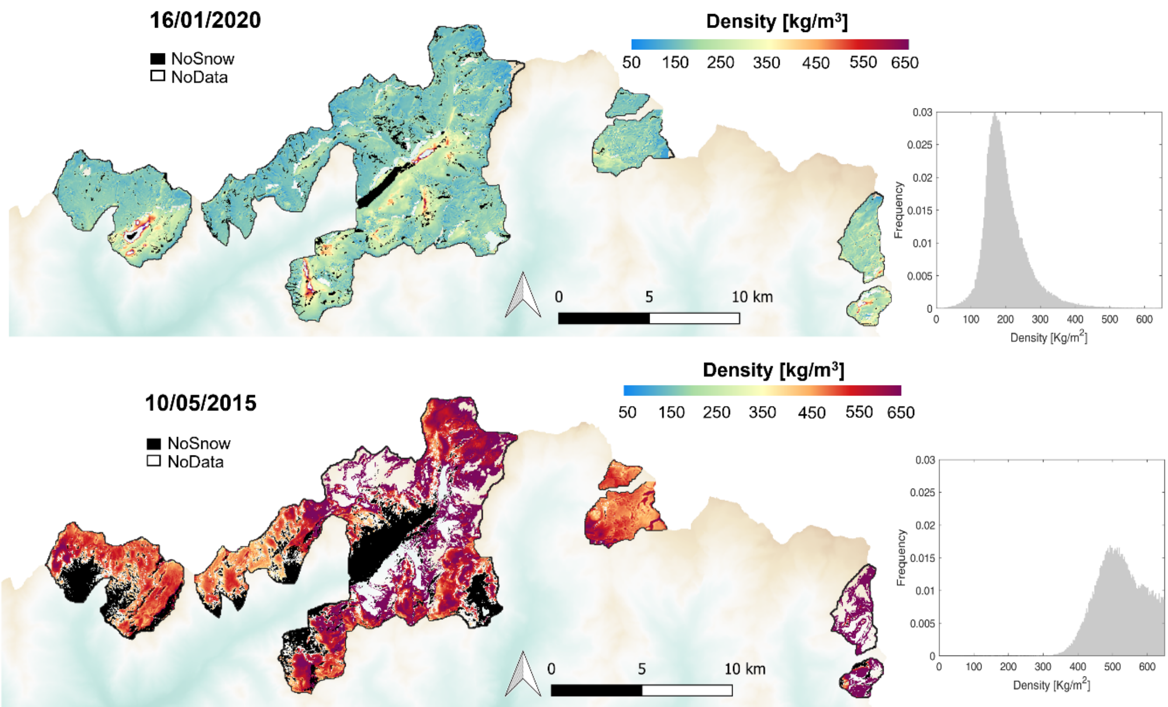

Figure 13: variability of surface snow density during the accumulation (16/01/2020) and melting (10/05/2015) seasons. Black represents no snow pixels, while NoData also includes surface snow density higher than 650 kg m^{-3}. The histograms underline the values distribution during these two periods for all the investigated catchments (the frequency is expressed from 0 to 1).

Although spatial variations in snow density occur within the catchments in these two periods, the seasonal variability is more pronounced. In January, in the accumulation period, the mean, median and mode values are equal to 200, 190 and 130 $\mathrm{kg\ m^{-3}}$, respectively. During melting, in May, snow density increases up to mean, median and mode values of 570, 560 and 480 $\mathrm{kg\ m^{-3}}$, respectively. For large APs values, the model produces erroneous estimates of snow density and all pixels with snow density greater than 650 $\mathrm{kg\ m^{-3}}$ should be taken with caution or discarded.

Besides these two periods, where most areas are in accumulation or melting, in the spring both processes may coexist and higher spatial variations in snow density can be observed. Figure 14a and b shows, for instance, the magnitude of spatial and interannual variability in snow density for the A-B transect in the Valpelline basin for all dates. For example, snow density exhibits different values in April 2020, encompassing a range of snow conditions, indicating areas where densification occurs differently. If we consider in the APs maps a threshold of 500 J m^{-2} K^{-1} $s^{-0.5}$, as a rough approach for distinguishing no melting snow and melting snow, we can observe that in April 2020 both conditions exist and the areas of melting represent 51% of the whole basin (Figure 14c). This simple threshold approach on APs may therefore help to separate cold dry snow or no melting snow with density values lower than 300 $\mathrm{kg\ m^{-3}}$ and to identify areas with higher snow density where snow is in melting (Figure 14d). This approach would allow a direct comparison with dry/wet snow maps derived from Synthetic Aperture Radar, such as Sentinel 1 (Marin et al. 2019) and Cosmo Skymed (Pettinato et al. 2013).

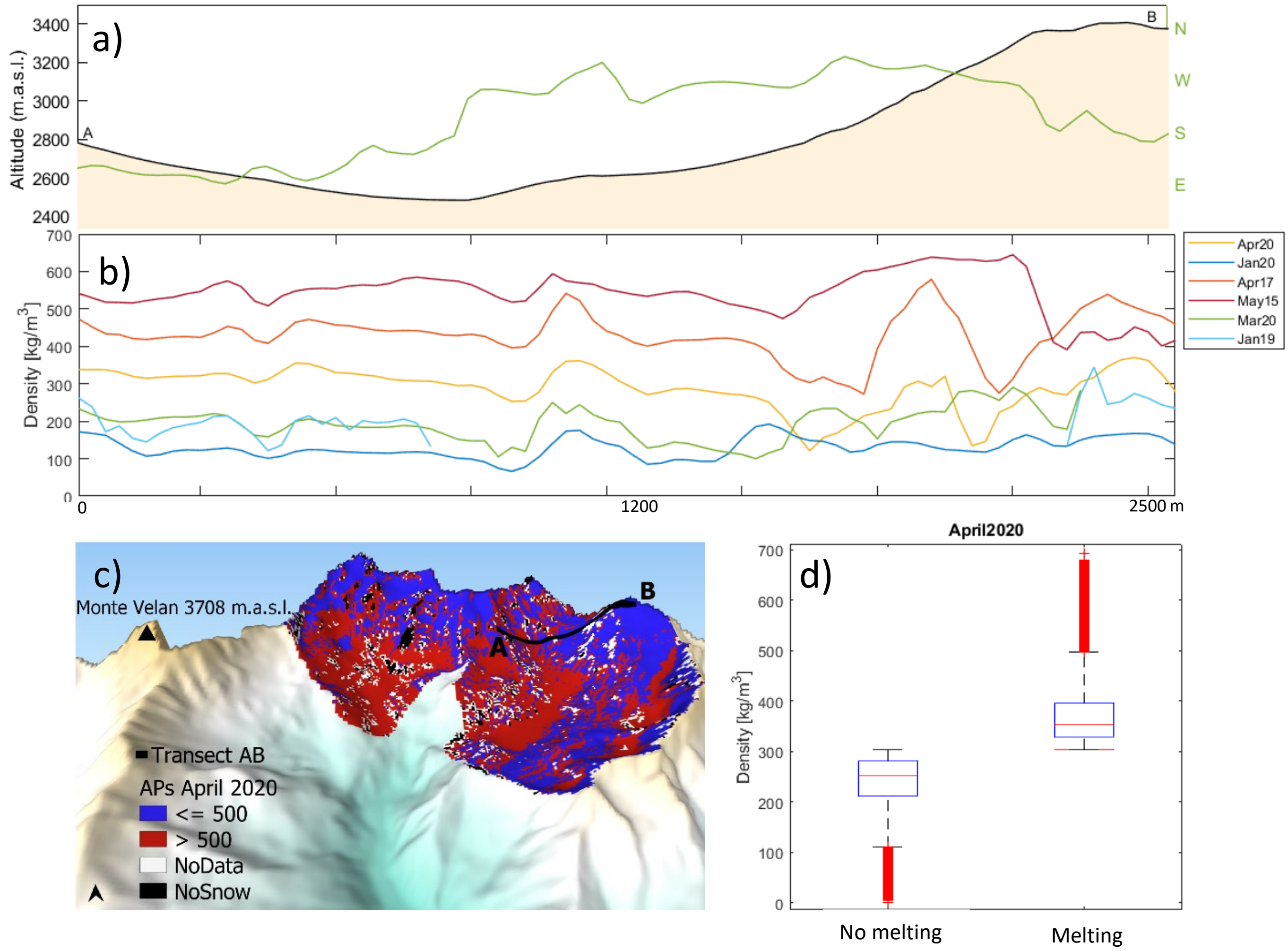

Figure 14 a) Altitudinal and aspect variability in a spatial transect in the Valpelline catchment; b) seasonal variability of snow density across the different dates; c) map of no melting and melting pixels overlapped on DEM and derived by applying a threshold (500 $Jm^{-2}K^{-1}s^{-0.5}$) to the APs map of April 2020; d) boxplot of snow density for all basins in April 2020.

Overall, we found significant temporal and spatial variability of snow density in the investigated catchments. Snow density evolution follows a seasonal pattern involving a gradual increase in snowpack density from winter to spring, when the maximum density is reached as a result of the multiple processes driving snow densification (compaction, metamorphism, melt and refreeze cycles). This is consistent with the findings reported in previous studies (Lopez-Moreno et al 2013; Jonas et al. 2009; Mizukami and Perica 2008; Pistocchi, 2016; Pomeroy and Gray 1995), which showed the spatial and temporal variability of snow density in response to different climatic regions and environmental factors. Although previous studies have argued that the density spatial variability is relatively small in comparison to snow depth (e.g., Mizukami and Perica, 2008), other studies have shown that snow density varies at the meter scale (Fassnacht et al., 2010; Grünewald et al., 2010) and caution should be taken when using density–time curves in mountainous regions (Bormann et al., 2013). Therefore, the perspective to map snow density from space could allow quantification of the spatial and temporal variability of snow in Alpine terrains in an unprecedented manner and could help to drive snow water equivalent models.

4. Limitations and improvements

This study has great potential to be improved and we are still far from proposing this method as an operational tool for estimating snow density using thermal inertia from space measurements. Although there are various sources of uncertainty, for which further research efforts are needed, the present approach represents a promising opportunity to map snow density variability in space and time. Here, we are more interested in presenting the general proof of concept and in demonstrating its potential, rather than developing or optimizing retrieval methods for deriving the input parameters for computing thermal inertia or suggesting new formulations of thermal inertia for snow purposes. All the input parameters and APs formulation are subject to uncertainties that affect the snow density estimates and further studies are needed to consolidate this approach.

A source of uncertainty of Td and SW_{in} maps comes from the use of an interpolation model from AWSs data. In our case, both interpolated dew point temperature and SW_{in} radiation values were generally underestimated by the MeteoIO model (data not shown) and this resulted in erroneous APs values. Global reanalysis data (e.g., ERA5 from the European Centre for Medium-Range Weather Forecasts, ECMWF) were discarded because of the coarse resolution (~30 km), which is unsuitable for tracking fine-scale snow dynamics in Alpine environments. Having frequent and high spatial resolution maps of meteorological parameters in rugged terrain still represents an important challenge for the future. Current downscaled reanalysis data (Di Mauro and Fugazza 2022) or spatially distributed snowpack simulations of mass and energy exchange (e.g., Revuelto et al., 2018) could help in bridging this gap. Accurate maps of incoming shortwave radiation are needed. Generally, when SW_{in} tends to very small values, ΔT tends to small values as a consequence, although with some temporal inertia. Furthermore, the geometric resampling introduced here may also be a source of error due to the complex topography of the study area. We also point out here that geolocation errors, due to the non-perfect spatial co-registration between the different sources of input data, can affect the pixel per pixel estimation of thermal inertia.

Spectral reflectance maps were obtained from ATCOR4 code, which considers atmosphere, sensor viewing geometry, terrain slope, shadowing and adjacency effects, which strongly influence radiometry data in rugged terrain. Despite adopting a physical-based approach, the estimation of ATCOR4-derived reflectance might benefit from a comparison with in situ reference measurements to assess the uncertainties related to atmospheric and topographic correction. Surface albedo estimates were only partially in agreement with those recorded on the ground from AWS. The assumptions underlying the narrow to broadband conversion, neglecting anisotropy and not properly accounting for cast shadows within the topographic correction process may explain the errors and uncertainties in the retrieved albedo. Different methods have recently been proposed to correct the effect of complex topography on snow spectral albedo (Picard et al. 2020). There is clearly a need to take into account the anisotropy of snow reflectance for mapping spatial albedo over time due to the dependence of snow reflectance on illumination-target-sensor geometry and snow properties (e.g., snow ages and grain coarsens). Overall, a generalisation of the estimation of bidirectional reflectance and snow albedo at high spatial resolution in complex terrain is still an open issue (Shuay et al., 2020) and this represents a key point in thermal inertia computation.

Regarding the ΔT maps, some elements can introduce errors and the estimates could be improved. Here, we are approximating the night-time surface temperature by the dew point temperature and this introduces some uncertainty. Landsat data provide good estimation of snow surface temperature during the day. Some inaccuracy may arise due to variable emissivity, which is expected to change with snow metamorphism, although snow emissivity is close to 1 (Hori et al 2006). The impact of topography on surface temperature can be more relevant since, in rugged terrain, surface temperature changes according to the variability of the atmospheric downwelling radiation (related to the local sky view factor) and from the different contributions of the surrounding terrain radiation. Different studies have simulated surface temperature over mountainous areas (Hais and Kucera, 2009; Dozier and Outcalt 1979; Malbéteau et al. 2017, Lipton 1997, Robledano et al. 2022, Firozjaei et al. 2020, Zhu et al., 2020) and an accurate and operational method to retrieve surface temperature in mountainous areas, which takes topography into account, is necessary for improving snow density estimates. It should also be noted that the measurements of surface temperature are instantaneous and hence subject to local changes of meteorological conditions, especially in mountainous terrain. Therefore, the interpretation of the surface temperature differences is not always straightforward in case of snow applications. Snow temperature is limited by 0 °C and, for example, a night-time dew point temperature close to freezing, could limit the applicability of our method. Overall, when ΔT is small, APs is difficult to interpret in terms of snow processes. Another point is the daily surface temperature mapping offered by Landsat, whose observations at 11.30 a.m. do not allow the detection of the maximum peak of temperature, which in this environment generally occurs in the early afternoon. It is likely, therefore, that ΔT differences are underestimated and the overall result could be more accurate if afternoon and minimum night-time measurements are considered. A simple approach using a cosine correction method (Scheidt, et al., 2010) applied to soils to shift surface temperature from 11.30 to 14.30 was also tested, but the difference in terms of APs was very small. However, additional studies in this direction should be pursued for remote sensing perspectives.

APs maps were obtained by using the first-order approximation Fourier series solution of the heat transfer equation, under the hypothesis that surface temperature has a sinusoidal behaviour. We previously tested this assumption at the point scale and sometimes, in the output phase, it is not always satisfied. In addition, snow temperatures might rise to freezing during warmer days later in the season, but be unable to get warmer because it is frozen, so that in this case the use of APs loses significance. Corrective factors could be included in new formulations of thermal inertia for snow applications, or the phase differences could be computed in different ways. We also tested other published formulations, including the second-order approximations, without finding better results (data not shown). Overall, several uncertain factors influence the accuracy of APs, and clear sky only at the time of the data acquisition, is not sufficient for accurate estimates of APs. We should also consider that thermal inertia describes the radiative regime in the upper snow layers only, so we expect a diurnal oscillation within the first 50 cm. This may limit the characterization of the snow density of the entire snowpack when using this approach. Moreover, the APs computed here does not perfectly match the true inertia Ps, and although in the accumulation and warming phases these quantities correspond, in the ripening and output phases they may differ when rapid melting and refreeze processes occur (Colombo et al., 2019). The theoretical model of Ps presented in Colombo et al. (2019) indeed predicts values from 100 J $m^{-2}K^{-1}s^{-0.5}$ for fresh fallen snow up to 1000 J $m^{-2}K^{-1}s^{-0.5}$ for wet snow and it shows that the influence of liquid water content has a weak effect on Ps. This range is consistent with the snow thermal inertia values defined by Cheruy et al. (2017) and with those found in this study, although a large overestimation may occur for water-saturated snow in the output phase. Overall, we found that APs clearly evolved during the hydrological season, with a certain spatial variability according to primary topographic parameters and driven by snow conditions. Particularly, APs is mainly a function of snow density. Higher values of apparent thermal inertia (e.g., > 500 J $m^{-2}K^{-1}s^{-0.5}$) may help in defining the extent of melting snow, while medium and low APs values are likely to represent drier snow. In general, the high APs range found in this study originally indicates that snow is a highly time-varying system, covering a wide range of inertia and encompassing typical values of dust, soils with different textures to higher values typical of pebbles, crust and rocks (e.g., Cheruy et al., 2017; Putzig and Mellon, 2007; Minacapilli et al., 2009; Sobrino and El Kharraz, 1999).

Overall, the derived snow density maps exhibit coherent seasonal patterns, with high variability during the spring and a certain variability according to the topography in the melting period. Spatial and temporal snow density patterns are consistent with the findings of other studies in similar contexts (e.g., Valt et al., 2018). However, the relationship between APs and snow density depends on a series of factors, such as snow conditions, time and site characteristics and needs to be locally calibrated. A better formulation of APs, which provide the same values of Ps throughout the season, could exploit a physical model, rather than empirical approaches, with the expectation of more satisfactory results in estimating snow density. Moreover, we underline that the generated snow density maps are not fully validated and further efforts should be made to evaluate the robustness of this approach and of the final estimates in different geographic contexts. Furthermore, it should be also considered that manual density measurements might also have uncertainties (Proksch et al., 2016) and therefore, more samples and replicates would be needed. Nevertheless, while the relationship we found could be improved, we believe that it can be considered significant (R^2_{CV} = 0.59 and $RMSE_{CV}$ = 82 $\mathrm{kg\ m^{-3}}$).

The remote estimation of thermal inertia may be a promising approach for estimating surface snow density and we are not aware of previous studies which combine optical and thermal data for the estimation of snow density. Further research could also concentrate on detecting snow density in mixed pixels and under vegetation canopies, which are not considered in this study. Patchy snow and heterogeneous pixels can produce erroneous APs values and hence inaccurate snow density results. Synergies with microwave systems should be pursued in these contexts, also to overcome issues related to cloud persistence and possibly to have information about the density within the overall snowpack.

Specific requirements for future satellite constellations focusing on cryosphere monitoring might include overpasses in the early afternoon, along with night-time acquisitions and daily revisit time at high spatial resolution. Overall, a revisit time of 1 day, with at least two nadir acquisitions at two different specific local times, and a multispectral payload in both visible and thermal channels (with a spatial resolution of 20-40 m and 40-60, in VNIR and TIR respectively), could constitute the main observational requirements for exploiting thermal inertia for snow density applications.

5. Conclusions

The estimation of snow density from thermal inertia could be a new frontier in remote sensing. We show preliminary evidence that snow density can be successfully estimated from APs observations. This may have an important impact on snow hydrology studies, mainly for determining the snow water equivalent at catchment scale in complex terrain. The possibility of mapping snow density through APs might represent a novel application for improved monitoring of the cryosphere and could potentially be used for freshwater resource management in the Alpine environment.

We used a hybrid approach to generate APs maps, starting from satellite images, meteorological modelling and field measurements and we developed an empirical regression model to estimate snow density in space and time. The goodness of the model seems to support the reliability and replicability of the proposed approach. We have, however, discussed elements of uncertainty and have proposed improvements to refine the methodology. To better assess the applicability of the method, it needs to be tested in a variety of study areas. Overall, we are confident that the maps of thermal inertia could help in detecting the onset of snowmelt and the snow density derived in different periods of the year, revealing consistent seasonal and spatial variability.

While this study may be the first step toward mapping and monitoring snow density from space, it may also help in defining the scientific requirements for new spaceborne missions targeting the cryosphere. We believe there is a need for a new class of satellites, with the ability to observe the Earth's surface at high spatial and temporal resolution, with both day and night-time overpasses in both optical and thermal domain. Such a mission, targeting snow dynamics at catchment scale, would be extremely relevant for continuously monitoring these ecosystems and for inferring quantitative information about hydrological resources and climate variability.

Credit author statement

Roberto Colombo: Conceptualization, Methodology, Investigation, Data curation, Writing - original draft, Funding acquisition. Greta Pennati: Investigation, Data curation. Giulia Pozzi: Investigation, Data curation. Roberto Garzonio: Conceptualization, Investigation, Data curation, Review & editing. Biagio Di Mauro: Conceptualization, Methodology, Funding acquistion, Review & editing. Claudia Giardino: Supervision, Methodology, Review & editing. Sergio Cogliati: Data curation, Investigation, Review & editing. Micol Rossini: Data curation, Review & editing. Antonino Maltese: Conceptualization, Methodology Review & editing. Paolo Pogliotti: Data curation. Edoardo Cremonese: Supervision, Methodology, Data curation, Review & editing.

Declaration of Competing Interest

The authors declare that they have no known competing financial interests or personal relationships that could have appeared to influence the work reported in this paper.

Acknowledgments

The study was supported by the MUSICA (Multiband Ultrawide SpectroImager for Cryosphere Analysis) project funded by the Italian Space Agency (ASI). Part of this work was supported by EU Horizon 2020 programme with the project Water-ForCE (GA n. 101004186).

We greatly acknowledge the Italian Space Agency (ASI), T. Scopa (ASI) and all project team for the discussion during the project. We also thank Dr. Gabriele Bramati for his inputs. Landsat images have been downloaded from https://earthexplorer.usgs.gov/. Digital Elevation model has been generated by the Aosta Valley Region and downloaded at https://geoportale.regione.vda.it/ricerche-tematiche/scheda/?id_tipo=3&uuid=r_vda%3A04257-META%3A20211020%3A100000).

We would like to thank the anonymous reviewers for their useful comments and suggestions.

References

- Andreas, E., L., 1986. A new method of measuring the snow-surface temperature, Cold Reg. Sci. Technol.,12(2), 139–156.
- Aït-Mesbah, S., Dufresne, J. L., Cheruy, F., Hourdin, F., 2015. The role of thermal inertia in the representation of mean and diurnal range of surface temperature in semiarid and arid regions. Geophysical Research Letters. 42, 7572–7580.
- Arenson, L., Colgan, W., Marshall, H. P., 2015. Physical, thermal, and mechanical properties of snow, ice, and permafrost. In Snow and ice-related hazards, risks, and disasters. 35-71. Elsevier.
- Aubry-Wake, C., Baraer, M., McKenzie, J. M., Mark, B. G., Wigmore, O., Hellström, R., et al., 2015. Measuring glacier surface temperatures with ground-based thermal infrared imaging. Geophysical Research Letters. 42, 8489–8497.
- Avanzi, F., Ercolani, G., Gabellani, S., Cremonese, E., Pogliotti, P., Filippa, G., et al., 2021. Learning about precipitation lapse rates from snow course data improves water balance modeling. Hydrology and Earth System Sciences, 25(4), 2109-2131.
- Bavay, M. and Egger, T., 2014. MeteoIO 2.4.2: a preprocessing library for meteorological data, Geosci. Model Dev. 7, 3135–3151.
- Bohn, N., Di Mauro, B., Colombo, R., Thompson, D.R., Susiluoto, J., Carmon, N. ,Turmon, M.J., Guanter, L., 2022. Glacier ice surface properties in South-West Greenland Ice Sheet: First estimates from PRISMA imaging spectroscopy data. J. Geophys. Res. Biogeosci, 127
- Bormann K. J., Seth Westra, Jason P. Evans, McCabe M F., 2013. Spatial and temporal variability in seasonal snow density, Journal of Hydrology. 484, , 63-73.
- Bormann, K. J., Brown, R. D., Derksen, C., Painter, T. H., 2018. Estimating snow-cover trends from space. Nature Climate Change. 8(11), 924–928.
- Brenning, A., Peña, M. A., Long, S., & Soliman, A. 2012. Thermal remote sensing of ice-debris landforms using ASTER: An example from the Chilean Andes. The Cryosphere. 6(2), 367–382.
- Broxton P.D., W.J.D. Leeuwen, Biederman J.A., 2019. Improving snow water equivalent maps with machine learning of snow survey and lidar measurements Water Resour. Res. 55 (5), 3739-3757.
- Carlson, T. Y., J. K. Dodd, S. G. Benjamin, and Cooper J. N., 1981. Satellite estimation of the surface energy balance, moisture availability and thermal inertia, J. Appl. Meteorol. 20, 67–87.
- Champollion, C., Deville, S., Chéry, J., Doerflinger, E., Le Moigne, N., Bayer, R., Mazzilli, N,. 2018. Estimating epikarst water storage by time-lapse surface-to-depth gravity measurements. Hydrology and Earth System Sciences. 22(7), 3825–3839.
- Cheruy, F., Dufresne, J. L., Aït Mesbah, S., Grandpeix, J. Y., Wang, F., 2017. Role of Soil Thermal Inertia in Surface Temperature and Soil Moisture-Temperature Feedback. Journal of Advances in Modeling Earth Systems. 9(8), 2906–2919.
- Colombo, R., Garzonio, R., Di Mauro, B., Dumont, M., Tuzet, F., Cogliati, S., Cremonese, E., 2019. Introducing Thermal Inertia for Monitoring Snowmelt Processes With Remote Sensing. Geophysical Research Letter. 46(8), 4308–4319.

- Di Mauro, B., Garzonio, R., Rossini, M., Filippa, G., Pogliotti, P., Galvagno, M., Colombo, R., 2019. Saharan dust events in the European Alps: Role in snowmelt and geochemical characterization. Cryosphere. 13(4), 1147–1165.
- Di Mauro, B., and Fugazza, D., 2022. Pan-Alpine glacier phenology reveals lowering albedo and increase in ablation season length, Remote Sens. Environ., 279, 113119.
- Dingman, S. L., 2015. Physical hydrology. Waveland Press, Inc. ISBN: 1–4786-1118-9.
- Dozier, J., and Outcalt, S. I., 1979. An Approach toward Energy Balance Simulation over Rugged Terrain. Geographical Analysis, 11(1), 65–85.
- Dozier, J., and Painter, T. H., 2004. Multispectral and hyperspectral remote sensing of alpine snow properties. Annual Review of Earth and Planetary Sciences. 32(1), 465–494.
- Fassnacht, S. R., Heun, C. M., López-Moreno, J. I., Latron, J., 2010. Variability of snow density measurements in the Rio Esera Valley, Pyrenees Mountains, Spain. Cuadernos de Investigacion Geografica, 36(1), 59–72.
- Firozjaei, M., K., Fathololoumi, S., Alavipanah, S. K., Kiavarz, M., Vaezi, A., R., Biswas, A., 2020. A new approach for modeling near surface temperature lapse rate based on normalized land surface temperature data. Remote Sensing of Environment. 242.
- Fukami, H., Kojima, K., Aburakawa, H., 1985. The Extinction and Absorption of Solar Radiation Within a Snow Cover. Annals of Glaciology. 6, 118–122.
- Green, R. O., Dozier, J., Roberts, D., Painter, T., 2002. Spectral snow-reflectance models for grain-size and liquid-water fraction in melting snow for the solar-reflected spectrum. Annals of Glaciology. 34(1), 71–73.
- Grünewald, T., Schirmer, M., Mott, R., Lehning, M., 2010. Spatial and temporal variability of snow depth and ablation rates in a small mountain catchment. Cryosphere. 4(2), 215–225.
- Hadley, O. L., Kirchstetter, T. W., 2012. Black carbon snow albedo reduction. Nature Climate Change. 2, 436-440.
- Hais, M. and Kucera, T., 2009 The Influence of Topography on the Forest Surface Temperature Retrieved from Landsat TM, ETM C and ASTER Thermal Channels. ISPRS Journal of Photogrammetry and Remote Sensing. 64, 585-591.
- Hall, D. K., Riggs, G. A., and Salomonson, V. V., 1995. Development of methods for mapping global snow cover using Moderate Resolution Imaging Spectroradiometer (MODIS) data. Remote Sensing Environment. 54, 127–140.
- Härer, S., Bernhardt, M., Siebers, M., & Schulz, K., 2018. On the need for a time- and location-dependent estimation of the NDSI threshold value for reducing existing uncertainties in snow cover maps at different scales. The Cryosphere, 12(5), 1629-1642.
- Hirashima, H., Abe, O., Sato, A., Lehning, M., 2009. An adjustment for kinetic growth metamorphism to improve shear strength parameterization in the SNOWPACK model. Cold Reg. Sci. Technol. 59, 169–177.
- Hori M., T. Aoki, T. Tanikawa, A. Hachikubo, K. Sugiura, K. Kuchiki, Niwano M., 2013. Modeling angular-dependent spectral emissivity of snow and ice in the thermal infrared atmospheric window. Appl. Opt. 52, 7243-7255.
- Hori M., Te. Aoki, T. Tanikawa, H. Motoyoshi, A. Hachikubo, K. Sugiura, T. Yasunari, H. Eide, R. Storvold, Y. Nakajima, Takahashi F., 2006. In situ measured spectral directional emissivity of snow and ice in the 8–14 µm atmospheric window. Remote Sens. Environ. 100, 486–502.

- Immerzeel WW, Lutz AF, Andrade M, Bahl A, Biemans H, Bolch T, Hyde S, Brumby S, Davies BJ, Elmore AC, et al., 2020. Importance and vulnerability of the world's water towers. Nature. 577(7790):364–369.
- Dumont M., Brissaud, O., Picard, G., Schmitt, B., Gallet, J.-C., Arnaud, Y. 2010. High-accuracy measurements of snow Bidirectional Reflectance Distribution Function at visible and NIR wavelengths - comparison with modelling results, Atmos. Chem. Phys., 10, 2507-2520.
- Järvinen, O., and Leppäranta, M., 2011. Transmission of solar radiation through the snow cover on floating ice. Journal of Glaciology. 57(205), 861–870.
- Jonas, T., Marty, C., Magnusson, J,. 2009. Estimating the snow water equivalent from snow depth measurements in the Swiss Alps. Journal of Hydrology. 378(1–2), 161–167.
- Kokhanovsky A., 2022. Light penetration in snow layers. Journal of Quantitative Spectroscopy and Radiative Transfer. 278.
- Kokhanovsky, A., Di Mauro, B., Garzonio, R., Colombo, R., 2021. Retrieval of Dust Properties From Spectral Snow Reflectance Measurements. Frontiers in Environmental Science. 9.
- Kokhanovsky, A., Lamare, M., Di Mauro, B., Picard, G., Arnaud, L., Dumont, M., et al., 2018. On the reflectance spectroscopy of snow. The Cryosphere. 12(7), 2371–2382.
- Kokhanovsky, A.; Lamare, M.; Danne, O.; Brockmann, C.; Dumont, M.; Picard, G.; Arnaud, L.; Favier, V.; Jourdain, B.; Le Meur, E.; Di Mauro, B.; Aoki, T.; Niwano, M.; Rozanov, V.; Korkin, S.; Kipfstuhl, S.; Freitag, J.; Hoerhold, M.; Zuhr, A.; Vladimirova, D.; Faber, A.-K.; Steen-Larsen, H.C.; Wahl, S.; Andersen, J.K.; Vandecrux, B.; van As, D.; Mankoff, K.D.; Kern, M.; Zege, E.; Box, J.E., 2019. Retrieval of Snow Properties from the Sentinel-3 Ocean and Land Colour Instrument. Remote Sens. 2019, 11, 2280.
- König, M., Winther, J.-G., Isaksson, E., 2001. Measuring snow and glacier ice properties from satellite. Reviews of Geophysics. 39(1), 1–27.
- Koren, V., Schaake, J., Mitchell, K., Duan, Q.-Y., Chen, F., Baker, J.M., 1999. A parameterization of snowpack and frozen ground intended for NCEP weather and climate models. J. Geophys. Res. D: Atmos. 104(D16), 19569–19585.
- Lacroix, P., Legresy, B., Remy, F., Blarel, F., Picard, G., Brucker, L., 2009. Rapid change of snow surface properties at Vostok, East Antarctica, revealed by altimetry and radiometry. Remote Sensing of Environment. 113(12), 2633–2641.
- Lastrada, E., Cobos, G., Garzón-Roca, J., Javier Torrijo, F. ,2021. Seasonal variability of snow density in the spanish pyrenees. Water. 13(11).
- Lemmetyinen, J., Schwank, M., Rautiainen, K., Kontu, A., Parkkinen, T., Mätzler, C., Wiesmann, A., Wegmüller, U., Derksen, C., Toose, P., Roy, A., Pulliainen, J., 2016. Snow density and ground permittivity retrieved from L-band radiometry: Application to experimental data. Remote Sensing of Environment. 180, 377–391.
- Liang, S., 2001. Narrowband to broadband conversions of land surface albedo I: Algorithms. Remote sensing of environment. 76(2), 213-238.
- Libois, Q., Picard, G., France, J. L., Arnaud, L., Dumont, M., Carmagnola, C. M., King, M. D., 2013. Influence of grain shape on light penetration in snow. Cryosphere. 7(6), 1803–1818.
- Lipton, A. E., Ward, J. M., 1997. Satellite-view biases in retrieved surface temperatures in mountain areas. Remote Sensing of Environment, 60(1), 92–100.
- Livneh, B., Xia, Y., Mitchell, K.E., Ek, M.B., Lettenmaier, D.P., 2010. Noah LSM snow model diagnostics and enhancements. J. Hydrometeorol. 11 (3), 721–738.

- López-Moreno, J., I., Fassnacht, S., R., Heath, J., T., Musselman, K., N., Revuelto, J., Latron, J., Morán-Tejeda, E., Jonas, T., 2013. Small scale spatial variability of snow density and depth over complex alpine terrain: Implications for estimating snow water equivalent. Advances in water resources. 55, 40-52.
- Malbéteau, Y., Merlin, O., Gascoin, S., Gastellu, J. P., Mattar, C., Olivera-Guerra, L., Jarlan, L., 2017. Normalizing land surface temperature data for elevation and illumination effects in mountainous areas: A case study using ASTER data over a steep-sided valley in Morocco. Remote Sensing of Environment. 189, 25–39.
- Maltese, A., Bates, P. D., Capodici, F., Cannarozzo, M., Ciraolo, G., La Loggia, G., 2013. Critical analysis of thermal inertia approaches for surface soil water content retrieval. Hydrological Sciences Journal. 58(5), 1144–1161.
- Marin, C., Bertoldi, G., Premier, V., Callegari, M., Brida, C., Hürkamp, K., Tschiersch, J., Zebisch, M., and Notarnicola, C., 2020. Use of Sentinel-1 radar observations to evaluate snowmelt dynamics in alpine regions, The Cryosphere, 14, 935–956.
- McCreight, J. L., & Small, E. E. , 2014. Modeling bulk density and snow water equivalent using daily snow depth observations. The Cryosphere, 8(2), 521-536.
- Meløysund, V., Leira, B., Høiseth, K.V., Lisø, K.R., 2007. Predicting snow density using meteorological data. Meteorol. Appl. 14 (4), 413–423.
- Minacapilli, M., Iovino, M., Blanda, F., 2009. High resolution remote estimation of soil surface water content by a thermal inertia approach. Journal of Hydrology. 379(3–4), 229–238.
- Mizukami, N., and Perica, S., 2008. Spatiotemporal characteristics of snowpack density in the mountainous regions of the Western United States. Journal of Hydrometeorology. 9(6), 1416–1426.
- Murray T., and Verhoef A., 2007. Moving towards a more mechanistic approach in the determination of soil heat flux from remote measurements: I. A universal approach to calculate thermal inertia. Agricultural and Forest Meteorology. 147, 1–2, 80-87.
- Naderpour, R., Schwank, M., Mätzler, C., 2017. Davos-Laret remote sensing field laboratory: 2016/2017 Winter season L-band measurements data-processing and analysis. Remote Sensing. 9(11).
- Naegeli, K., Damm, A., Huss, M., Wulf, H., Schaepman, M., Hoelzle, M., 2017. Cross-comparison of albedo products for glacier surfaces derived from airborne and satellite (Sentinel-2 and Landsat 8) optical data. Remote Sensing. 9(2).
- Nearing, G. S., Moran, M. S., Scott, R. L., Ponce-Campos, G., 2012. Coupling diffusion and maximum entropy models to estimate thermal inertia. Remote Sensing of Environment. 119, 222–231.
- Oesch, D., Wunderle, S., Hauser, A., 2002. Snow surface temperature from AVHRR as a proxy for snowmelt in the Alps. Proceedings of EARSeL-LISSIG-Workshop, Observing our Cryosphere from Space, Bern Vol. 164.Oke, T. R., 1987. Boundary layer climates. Routledge.
- Oldroyd, H. J., Higgins, C. W., Huwald, H., Selker, J. S., Parlange, M. B., 2013. Thermal diffusivity of seasonal snow determined from temperature profiles. Advances in water resources. 55, 121-130.
- Onuchin, A.A., Burenina, T.A., 1996. Climatic and geographic patterns in snow density dynamics. Northern Eurasia. Arctic Alpine Res. 28 (1), 99–103.

- Painter, T. H., Seidel, F. C., Bryant, A. C., McKenzie Skiles, S., Rittger, K., 2013. Imaging spectroscopy of albedo and radiative forcing by light-absorbing impurities in mountain snow. Journal of Geophysical Research: Atmospheres. 118(17), 9511-9523.
- Paruta, A., P. Nasta, G. Ciraolo, F. Capodici, S. Manfreda, N. Romano, E. Bendor, Y. Zeng, S. F. Dal Sasso and R. Zhuang, A. Maltese. 2021, A geostatistical approach to map near-surface soil moisture through hyper-spatial resolution thermal inertia, IEEE Transactions on Geoscience and Remote Sensing. . 59, 6, 5352-5369.
- Perovich, D. K., 2007. Light reflection and transmission by a temperate snow cover. Journal of Glaciology. 53(181), 201–210.
- Pettinato S., Santi, E., Brogioni M., Paloscia S., Palchetti E., Xiong, C., 2013. The Potential of COSMO-SkyMed SAR Images in Monitoring Snow Cover Characteristics, in IEEE Geoscience and Remote Sensing Letters, vol. 10, no. 1, pp. 9-13.
- Picard, G., Dumont, M., Lamare, M., Tuzet, F., Larue, F., Pirazzini, R., and Arnaud, L., 2020. Spectral albedo measurements over snow-covered slopes: theory and slope effect corrections, The Cryosphere, 14, 1497–1517.
- Pistocchi, A., 2016. Simple estimation of snow density in an Alpine region. Journal of Hydrology: Regional Studies. Volume 6, 82-89.
- Pomeroy, J., W., and Gray, D., M., 1995. Snow Accumulation, Relocation and Management. NHRI Science Report No. 7. National Hydrology Research Institute, Saskatoon.Pratt, D., A. and Ellyett, C. D., 1979. The thermal inertia approach to mapping of soil moisture and geology. Remote Sensing of Environment, 8: 151–168.
- Price, J., C., 1980. The potential of remotely sensed thermal infrared data to infer surface soil moisture and evaporation. Water Resources Research. 16(4), 787–795.
- Proksch, M., Rutter, N., Fierz, C., and Schneebeli, M., 2016. Intercomparison of snow density measurements: bias, precision, and vertical resolution. The Cryosphere. 10, 371–384.
- Putzig, N. E., and Mellon, M. T., 2007. Apparent thermal inertia and the surface heterogeneity of Mars. Icarus. 191(1), 68–94.
- Raleigh, M. S., and Small, E. E., 2017. Snowpack density modeling is the primary source of uncertainty when mapping basin-wide SWE with lidar. Geophysical Research Letters, 44, 1-10.
- Raleigh, M. S., Landry, C. C., Hayashi, M., Quinton, W. L., Lundquist, J. D., 2013. Approximating snow surface temperature from standard temperature and humidity data: New possibilities for snow model and remote sensing evaluation. Water Resources Research. 49(12), 8053–8069.
- Ren, S., Miles, E. S., Jia, L., Menenti, M., Kneib, M., Buri, et al., 2021. Anisotropy parameterization development and evaluation for glacier surface albedo retrieval from satellite observations. Remote Sensing. 13(9).
- Revuelto, J.; Lecourt, G.; Lafaysse, M.; Zin, I.; Charrois, L.; Vionnet, V.; Dumont, M.; Rabatel, A.; Six, D.; Condom, T.; Morin, S.; Viani, A.; Sirguey, P. 2018. Multi-Criteria Evaluation of Snowpack Simulations in Complex Alpine Terrain Using Satellite and In Situ Observations.Remote Sens., 10, 1171.Richter, R., Schläpfer, D., 2015. Atmospheric/Topographic Correction for Airborne Imagery (ATCOR-4 User Guide), Langeggweg, Switzerland.
- Robledano, A., Picard, G., Arnaud, L., Larue, F., and Ollivier, I., 2022. Modelling surface temperature and radiation budget of snow-covered complex terrain, The Cryosphere, 16, 559–579.

- Roy, A., Toose, P., Williamson, M., Rowlandson, T., Derksen, C., Royer, A., et al., 2017. Response of L-Band brightness temperatures to freeze/thaw and snow dynamics in a prairie environment from ground-based radiometer measurements. Remote Sensing of Environment. 191, 67–80.
- Scheidt, S., Ramsey, M., and Lancaster, N., 2010. Determining soil moisture and sediment availability at White Sands Dune Field, New Mexico, from apparent thermal inertia data. Journal of Geophysical Research. 115, 1–23
- Schwank, M., and Naderpour, R., 2018. Snow density and ground permittivity retrieved from L-band radiometry: Melting effects. Remote Sensing. 10(3), 354.
- Schwank, M., Mätzler, C., Wiesmann, A., Wegmüller, U., Pulliainen, J., Lemmetyinen, J., Rautiainen, K., Derksen, C., Toose, P., Drusch, M., 2015. Snow density and ground permittivity retrieved from L-band radiometry: A synthetic analysis. IEEE Journal of Selected Topics in Applied Earth Observations and Remote Sensing. 8(8), 3833-3845.
- Shi, J., and Dozier, J., 2000. Estimation of snow water equivalence using SIR-C/X-SAR, Part I: Inferring snow density and subsurface properties. IEEE Transactions on Geoscience and Remote Sensing. 38(6), 2465–2474.
- Short, N., M., Stuart, L., M., 1982. The heat capacity mapping mission (HCMM) anthology. NASA SP-465, (p. 264). Washington, D.C: NASA.
- Shuai, Y., Tuerhanjiang, L., Shao, C., Gao, F., Zhou, Y., Xie, et al., 2020. Re-understanding of land surface albedo and related terms in satellite-based retrievals. Big Earth Data. 4(1), 45-67.
- Skiles, S., M., Flanner, M., Cook, J. M., Dumont, M., Painter, T. H., 2018. Radiative forcing by light-absorbing particles in snow. Nature Climate Change. 8(11), 964–971.
- Snehmani, Venkataraman, G., Nigam, A. K., Singh, G., 2010. Development of an inversion algorithm for dry snow density estimation and its application with ENVISAT-ASAR dual co-polarization data. Geocarto International. 25(8), 597–616.
- Sobrino, J. A., and El Kharraz, M. H., 1999. Combining afternoon and morning NOAA satellites for thermal inertia estimation. 1. Algorithm and its testing with Hydrologic Atmospheric Pilot Experiment-Sahel data. Journal of Geophysical Research Atmospheres, 104(D8), 9445–9453.
- Sobrino, J. A., El Kharraz, M. H., Cuenca, J., Raissouni, N., 1998. Thermal inertia mapping from NOAA-AVHRR data. Advances in Space Research. 22(5), 655-667.
- Sturm, M., Taras, B., Liston, G. E., Derksen, C., Jonas, T., Lea, J., 2010. Estimating snow water equivalent using snow depth data and climate classes. Journal of Hydrometeorology. 11(6), 1380–1394.
- Svoma B.M., 2011. Winter climatic controls on spring snowpack density in the Western United States. Arctic, Antarctic and Alpine Research. 43: 118-126.
- Thakur, P. K., Aggarwal, S. P., Garg, P. K., Garg, R. D., Mani, S., Pandit, A., Kumar, S., 2012. Snow physical parameters estimation using space-based synthetic aperture radar. Geocarto International. 27(3), 263–288.
- Valt M., Romano E., Guyennon N., 2018. Snow cover density and snow water equivalent in the Italian Alps. Proceedings, International Snow Science Workshop, Innsbruck.
- Van Doninck, J., Peters, J., De Baets, B., De Clercq, E. M., Ducheyne, E., Verhoest, N. E. C., 2011. The potential of multitemporal Aqua and Terra MODIS apparent thermal inertia as a soil moisture indicator. International Journal of Applied Earth Observation and Geoinformation. 13(6), 934–941.

- Wang, J., Bras, R. L., Sivandran, G., Knox, R. G., 2010. A simple method for the estimation of thermal inertia. Geophysical Research Letters. 37(5).
- Wang, K., and Liang, S., 2009. Estimation of daytime net radiation from shortwave radiation measurements and meteorological observations. Journal of Applied Meteorology and Climatology. 48(3), 634–643.
- Xue, Y., and Cracknell, A. P., 1995. Advanced thermal inertia modelling. International Journal of Remote Sensing, 16(3), 431–446.
- Zhong, E., Li, Q., Sun, S., Chen, S., Chen, W., 2017. Analysis of euphotic depth in snow with SNICAR transfer scheme. Atmospheric Science Letters. 18(12), 484–490.

Zhu, X., Duan, S. B., Li, Z. L., Zhao, W., Wu, H., Leng, P., Gao, M., Zhou, X., 2020. Retrieval of land surface temperature with topographic effect correction from Landsat 8 thermal infrared data in mountainous areas. IEEE Transactions on Geoscience and Remote Sensing.